



Intermittency patterns in the chaotic transition of the planar flow past a circular cylinder

D. Durante  and C. Pilloton 

CNR-INM, Institute of Marine Engineering, Via di Vallerano 139, 00128 Rome, Italy

A. Colagrossi *

CNR-INM, Institute of Marine Engineering, Via di Vallerano 139, 00128 Rome, Italy
and Ecole Centrale Nantes, LHEEA Research Department (ECN and CNRS),
1 rue de la Noë, 44321 Nantes Cedex 3, France



(Received 26 July 2021; accepted 14 April 2022; published 24 May 2022)

The present paper investigates the planar flow past a circular cylinder for Reynolds numbers between 1000 and 10 000. The flow is studied as a dynamical system, so the present investigation is motivated by the presence of complex patterns, as the Reynolds number increases, in the force-time signals when the system goes from the periodic to the chaotic regime. The 2D numerical simulations were performed with a Lagrangian particle method called diffused vortex hydrodynamics (DVH). This computational approach allows high spatial resolutions with an accurate description of different vortical scales shed in the flow field. Flow analysis was executed with the typical tools used in the study of dynamical systems (i.e., Fourier spectra, Poincaré sections, and phase space maps) and is supported by discussion of the near and far wake topologies. During the transition of the system from a regular to a chaotic regime, the lift time signal shows intermittent irregular patterns.

DOI: [10.1103/PhysRevFluids.7.054701](https://doi.org/10.1103/PhysRevFluids.7.054701)

I. INTRODUCTION

In recent years the study of planar flow patterns past immersed bodies has gained a renewed interest. Improvements in experimental technologies such as flowing soap film apparatuses combined with the use of a high-speed camera and low-pressure sodium lamp allowed the visualization of complex interference patterns (see, for example, Fayed *et al.* [1]). These kinds of devices are also widely used for the visualization of the planar flow of the vortical wake of flapping foils (Schnipper *et al.* [2]) or of a flexible filament subject to a forced vibration (Jia *et al.* [3]). In connection with the experimental investigations, many numerical studies on planar flow past fixed, moving, or deformable frontiers can be found in the recent literature (see, e.g., Badrinath *et al.* [4], Bose and Sarkar [5], Das *et al.* [6], Krishnan *et al.* [7], Mandujano and Málaga [8], Reichl *et al.* [9], and Ye *et al.* [10]).

Studies on these problems are motivated by a wide field of application. An example is the free-surface flows at low Froude number and high Reynolds number (e.g., flow with a low velocity/reference length ratio, such as the one generated by a moving ship in a harbour or by bridge piers in slow currents as shown in Fig. 1). These flows are essentially two-dimensional because the vorticity dynamics affects mainly the air-water interface.

An extensive literature on the flow past a circular cylinder was produced during the last century, exploiting theoretical and experimental approaches. In the past three decades the adoption of different numerical strategies became a further tool of investigation.

*andrea.colagrossi@cnr.it

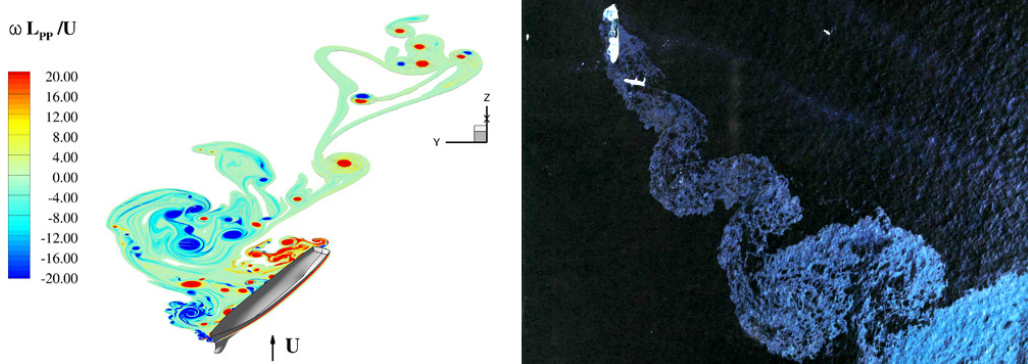


FIG. 1. Left: wake shed by a ship model of length 2 m and advancing in drift at 0.2 m/s. Colours are representative of the vertical component of the vorticity. Right: wake pattern of the tanker *Argo Merchant* inclined about 45° to the current and leaking crude oil (NASA photograph) (see Ref. [11]).

One of the pioneering studies on this topic was carried out by Zdravkovich [12], which offered fundamentals of the problem together with an overview of different methods of analysis. A classification of the different flow fields obtained by varying the Reynolds number (Re hereafter) highlighted various flow regimes. Despite the three-dimensional (3D) nature of the flow field, similar classifications are also detectable in a two-dimensional (2D) framework also for high Reynolds numbers. Some key mechanisms such as the *drag crisis*, where the flow transition affects the boundary layer and the drag force sudden drops, are also observed in 2D, although the drop is anticipated at $Re = 50\,000$ rather than at $300\,000$ as in 3D (see Singh and Mittal [13] or Durante *et al.* [14]). Similarly, the investigation of the turbulence transition for the planar flow past a circular cylinder (Durante *et al.* [14]) led to the identification of transition eddies in the shear layer during the intermediate subcritical regime at Re around 5×10^4 , as in the 3D counterpart.

The present investigation follows recent studies on the planar flow past elliptic (Durante *et al.* [15]) and NACA profiles (Durante *et al.* [16]), where typical tools of dynamical systems analysis (i.e., Fourier spectra, Poincaré sections, phase maps, and Lyapunov exponents) were exploited to characterize different flow regimes.

Here, the transition of the planar flow past a circular cylinder in the Reynolds number range 1000 – $10\,000$ is investigated with a particular emphasis on the range 3000 – 4000 , where the flow is observed to pass from an almost regular to a chaotic regime. In the range of Re 150 – 1000 , Jiang and Cheng [17] investigated the wake dynamics to quantify the transition from primary to secondary vortex streets while in Dynnikova *et al.* [18], with Re varying between 140 and 1000 , the flow properties were explored with a vortex method.

In chaotic transition studies, the investigation is typically performed through the use of the time signal of the transversal velocity obtained in some points of the near wake rather than of the streamwise component, which is found to be noisy (see, for example, Pulliam and Vastano [19] or Saha *et al.* [20]). A significant arbitrariness remains about the choice of probe locations in the wake, which may lead to incorrect conclusions about the chaotic transition of the system. To overcome this ambiguity, we prefer to consider the lift force because it is independent of any specific location within the flow field. It is a global quantity related to the vorticity momenta of the whole field (see, e.g., Graziani and Bassanini [21]) and it oscillates roughly at half the frequency of the drag force.

In the present work the adoption of a recently developed Particle Vortex Method, called diffused vortex hydrodynamics (DVH), enabled the investigation of the vorticity dynamics with a high level of accuracy and for long simulation times. This approach provides a detailed description of the vortical part of the two-dimensional viscous isochoric flow field around a body. The DVH numerical code, described in detail in Rossi *et al.* [22,23], is coupled with a packing algorithm coming from

smoothed particle hydrodynamics, (SPH), which allows a regular distribution of the points around a solid surface, correctly enforcing the no-slip boundary condition on the body. It is worth stressing that in the present approach no subgrid-scale model is used because the numerical scheme is able to solve the entire spectrum of the vorticity scales.

The paper is organized as follows: in Sec. II the DVH model is briefly recalled and the problem is outlined; in Sec. III the periodic case at $Re = 1000$ is described; in Sec. IV the modulating cases $Re = 2000$ and $Re = 3000$ are investigated; in Sec. V the cases where the intermittency patterns appear were described in detail; in Sec. VI the chaotic cases are shown, while in Sec. VII the Lyapunov exponents and the averaged drag coefficients are discussed. Finally, conclusions wrap up the article in Sec. VIII.

II. SUMMARY OF THE NUMERICAL METHOD AND PROBLEM OUTLINE

A. The diffused vortex hydrodynamics model

In this section a brief description of the adopted particle vortex method is outlined. The method is based on the viscous incompressible Navier-Stokes equations, rewritten in vorticity form (also known as Helmholtz equations), in the two-dimensional domain Ω :

$$\rho \frac{D\omega(\mathbf{r}, t)}{Dt} = \mu \Delta \omega(\mathbf{r}, t), \quad \text{with } \mathbf{r} \in \Omega, \quad t \in [0, +\infty), \quad (1)$$

where ω is the planar vorticity, D/Dt is the material time derivative and ρ and μ are the density and the dynamic viscosity of the fluid.

Equation (1) is integrated in time according with the splitting technique described by Chorin [24,25], where the advection and the diffusion steps are separately considered at each time instant.

More specifically, the inviscid advective step is described by the Euler equation:

$$\frac{D\omega(\mathbf{r}, t)}{Dt} = 0, \quad (2)$$

followed by the diffusive equation:

$$\rho \frac{\partial \omega(\mathbf{r}, t)}{\partial t} = \mu \Delta \omega(\mathbf{r}, t). \quad (3)$$

To take into account the presence of a solid body, the vorticity generated on the body contour is considered between the advection and the diffusion steps so that the no-slip boundary conditions are correctly enforced.

According to Chorin [24], the vorticity field may be described as a discrete distribution of point vortices:

$$\omega(t, \mathbf{r}) = \sum_{j=1}^N \Gamma_j(t) \delta_\varepsilon(\mathbf{r} - \mathbf{r}_j), \quad (4)$$

where δ_ε is a positive smooth approximation of the Dirac function such that $\delta_\varepsilon \rightarrow 0$ when $\varepsilon \rightarrow 0$, also known as *mollifier* or kernel function (see also Rossi *et al.* [22]). Each Lagrangian point \mathbf{r}_j associated with a specific circulation Γ_j is referred to as a *vortex particle*.

During the advective step, the velocity field is decomposed into three components: $\mathbf{u} = \mathbf{u}_\infty + \mathbf{u}_\omega + \mathbf{u}'$, where \mathbf{u}_∞ is the free stream velocity, \mathbf{u}_ω is the velocity induced by the vortex particles, while \mathbf{u}' is the contribution to the velocity field coming from the body.

The velocity \mathbf{u} is evaluated through a Fast Multiple Method (FMM) (see, e.g., Ref. [26]) and the vortices are then moved using a fourth order Runge-Kutta algorithm. From \mathbf{u}' it is also possible to generate a new set of vortices on the body surface, enforcing the no-slip boundary conditions exactly over its contour. The present formulation has several advantages:

- (i) it requires the discretization of the rotational region only of the flow field;
- (ii) the asymptotic boundary conditions are automatically satisfied;
- (iii) the vortex particles are moved in a Lagrangian way.

The diffusive step is carried out in accordance with the deterministic algorithm of Benson *et al.* [27]: each vortex particle diffuses its vorticity on a “regular point distribution” (RPD) through a superposition of elementary solutions of the heat equation. This set of points afterwards becomes the new set of vortex particles replacing the old ones. The use of RPDs during the diffusion process also prevents the excessive clustering or rarefaction of the vortex particles and avoids remeshing procedures that are otherwise required (see, e.g., Barba *et al.* [28]). The RPDs are generated using the packing algorithm described in Colagrossi *et al.* [29], allowing the arrangement of the points around complex contours by maintaining an almost constant distance between them.

The present model is named diffused vortex hydrodynamics (DVH). Since the RPDs are sets of points regularly spaced without any topological connection the DVH scheme can be considered a pure meshless methods. The DVH has been extensively validated and further details can be found in Colagrossi *et al.* [30], Durante *et al.* [14], Giannopoulou *et al.* [31], Rossi *et al.* [22,23,32,33]. Thanks to the description in terms of vorticity [see Eq. (1)], the computational costs of the DVH are generally smaller if compared to classical mesh-based methods. Moreover, the algorithm is further supported by an adapt particle resolution (APR) technique, which allows one to gradually scale down the particle size in the near-field [22]. Using the APR, the whole wake is retained during the simulation time without the use of an outflow boundary.

In the present study, long-time simulations were carried out, both due to the presence of very long transients and the intermittency phenomena. During these time intervals, the force time signal shifts from regular to irregular time behavior. To assess those changes in the flow dynamics, about 100 oscillations need to be taken into account. To the authors’ knowledge, there are no studies in the literature dealing with long-time simulations in the Reynolds number range 1000–10 000.

B. CPU costs

The simulations were all performed on a Workstation equipped with 96 cores (Dual Gold Intel Xeon 6252 processors 2.10 GHz), through an OpenMP parallel interface programming. The CPU costs of the implemented algorithm for 2D cases are about 100 μ s per vortex particle and per time iteration on a single core. It is worth stressing that, although the analysis carried out in the present work is confined to a two-dimensional framework, the fine spatial resolutions adopted, as well as the long-time evolution, determined demanding computational costs. Indeed, to perform the 19 simulations presented here, each of them with about 2 million vortices for 60 000 time iterations, the net computational cost, excluding the post processing, was about 2 months. This cost is aligned with other vortex particle solvers and it is mainly affected by the fast multipole method used for the solution of the Poisson equation; indeed the largest number of used particles is of order 10^6 and the allocated memory is not higher than 1 Gbyte. If a similar computation were performed for an extension of the analysis in a 3D framework, it would require about 2 billion particles considering the same spatial resolution as that adopted for 2D simulations. Hence, the CPU costs remain nowadays prohibitive in terms of numerical resources.

C. Outline of the problem

In the present work the planar incompressible flow past a circular cylinder is considered. The cylinder diameter c , as reference length, is set equal to 1. The numerical method adopted is a meshless method, where open boundaries are implicitly assumed. The free stream U_∞ grows from 0 to 1 in t_r^* nondimensional time units ($t^* = tU/c$) to avoid numerical instabilities, according to the time law used in Giannopoulou *et al.* [31] and recalled here:

$$U_\infty(t) = \begin{cases} \frac{U}{2} \left[1 - \cos\left(\frac{\pi t^*}{t_r^*}\right) \right] & t^* \leq t_r^* \\ U & t^* > t_r^* \end{cases} \quad t_r^* = 2U/c, \quad (5)$$

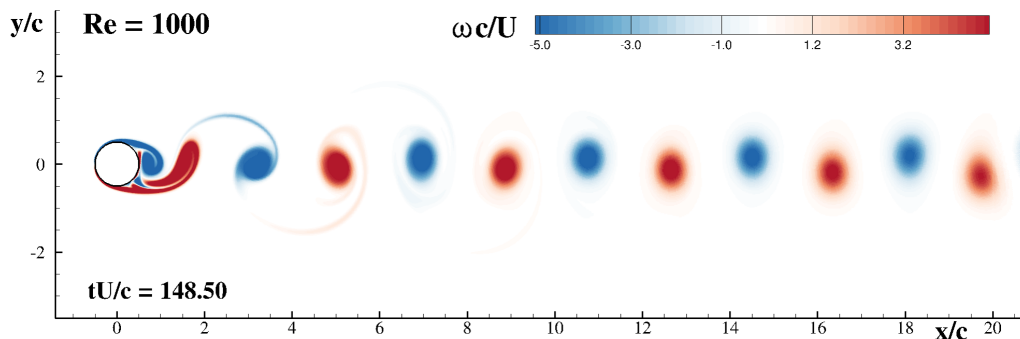


FIG. 2. Cylinder vorticity wake for $Re = 1000$ case at maximum lift, see Supplemental Material [44].

where U is the stream velocity and c the cylinder diameter. The Reynolds number, the drag and the lift coefficients are here defined as

$$Re = \frac{Uc}{\nu}, \quad C_D = \frac{D}{\frac{1}{2}\rho U^2 c^2}, \quad C_L = \frac{L}{\frac{1}{2}\rho U^2 c^2},$$

where ρ and ν are the density and the kinematic viscosity of the fluid, respectively. The forces D and L are the drag and lift acting on the cylinder, i.e., the force components along and transverse to the free stream, respectively.

The vortex particle method's accuracy strictly depends on the number of vortices generated at every time step (see Rossi *et al.* [22]), which are in turn related to the Reynolds number used in the simulations. With the increase in the Reynolds number from 1000 to 10 000, the number of vortices per unit of length increases accordingly. In this way the entire vorticity spectrum is resolved up to the diffusive scale.

III. NONMODULATING CASE: $Re = 1000$

The present analysis starts from the periodic case (shown in Durante *et al.* [14] and Singh and Mittal [13]), to outline the strategy of investigation. At $Re = 1000$ the time signal of force, after a transient, becomes periodic (although nonmonochromatic). The regular vortex shedding, shown in Fig. 2, induces a regular pattern in the lift behavior, as evidenced in the left frame of Fig. 3. The low-frequency modulation, observed for higher Reynolds numbers, is here absent. The vortex wake is characterized by distinct vortex patches weakly interacting up to 20 diameters from the body surface. The Fourier transform, plotted in Fig. 3 on the right of the force time signal, shows a discrete peak distribution of the amplitudes. Each peak corresponds to the odd higher harmonics (indicated with a red circle and the corresponding harmonic number) of the principal one (indicated with **1**), thus suggesting that the lift signal is a periodic function with odd half-wave symmetry

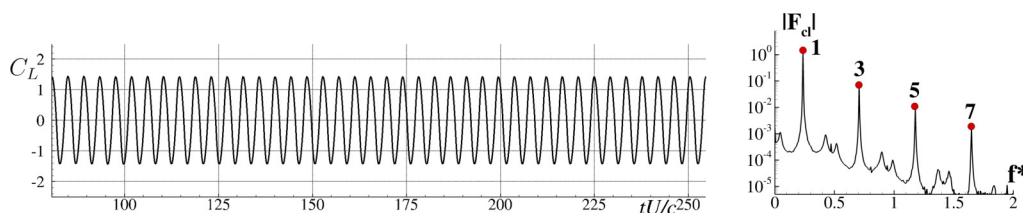


FIG. 3. Lift time signal at regime conditions and corresponding Fourier analysis for $Re = 1000$ case. The dominant and higher harmonics are highlighted with red circles.

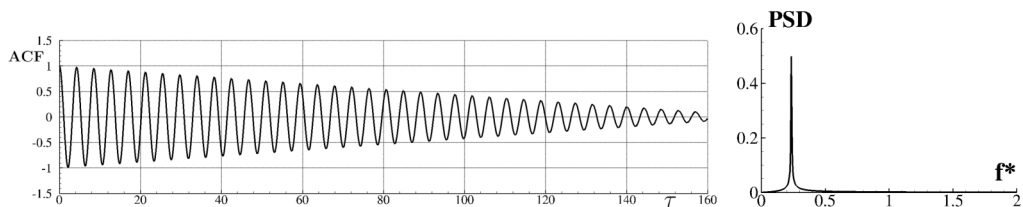


FIG. 4. Autocorrelation function for $Re = 1000$ case and corresponding PSD, where τ indicates the nondimensional time lag of the signal.

(Sundararajan [34]). The high spatial resolutions achieved with the DVH approach allow a very regular lift signal to be obtained, with the higher amplitudes of the spectrum correctly placed at integer multiples of the fundamental one. This behavior is typically associated with a regular vortex shedding and it was also found for an ellipse with an aspect ratio of 0.4 and zero angle of attack in Durante *et al.* [15], but for a higher and wide Reynolds number range (i.e., $3000 \leq Re \leq 10\,000$).

The autocorrelation function of the lift signal, depicted in Fig. 4, shows a signal that is highly self-correlated up to 100–120 time lags. In fact, it reveals behavior that one would expect from a periodic function (i.e., clear presence of a repeating pattern). By exploiting the Wiener-Khinchin theorem (for further details see Wiener [35]), the power spectral density (PSD) was deduced from the autocorrelation function in the left frame of Fig. 4. The right frame of the same figure explains how the signal power is distributed over the frequency range, showing again that the shedding frequency (in this case $f^* = fc/U \simeq 0.2355$) is the one mainly associated with the signal power.

The phase maps, or phase portraits, are geometric representations of the trajectories of a dynamical system in the phase plane. In the present work, similarly to Durante *et al.* [16], the phase space considered is the $(C_L, \dot{C}_L, \ddot{C}_L)$, where the dot stands for the time derivative, which was found to give an appropriate description of the system transition from regular to chaotic regimes. Taking into account the section in which $\dot{C}_L = 0$, the plane (\ddot{C}_L, C_L) with $\dot{C}_L < 0$ depicts the maxima of the lift signal, highlighting the bifurcations that occur with the increase in the Reynolds number (see, for example, Durante *et al.* [16], Pulliam and Vastano [19]).

In Fig. 5 the phase map and the Poincaré section for the $Re = 1000$ case are depicted in the top-left and bottom-right frames, respectively. In the top-right, a 3D representation of the phase map is depicted using the time coordinate. This portrayal clarifies the time behavior of the phase map, as well as the contouring used for the corresponding curve (darker with time).

The phase map related to a periodic signal (the regime reported in Fig. 3) shows a stable orbit, as expected, indicating a periodic trend of the forces acting on the cylinder.

It is worth stressing that this aspect is directly related to the integral of the first momentum of the vorticity, as clarified in the next section. Although the whole vorticity field plays a role in the force behavior, the regular vortex shedding in the near and mean wake seems to be more likely related to the periodic oscillation of the lift signal, whereas in the far field the mutual interaction between the shed vortices may trigger the wake to move toward a chaotic condition.

The absence of a modulation in the lift signal makes its oscillations very similar, in such a way that their amplitude, as well as their concavity, are almost identical. This is depicted by the Poincaré section in the right frame of Fig. 5 that coherently shows one group of clustered points related to the lift maxima.

To clarify the extraction of the Poincaré section, Fig. 5 is enriched with the 3D plots of the curve $[C_L(t), \dot{C}_L(t)]$ with time, showing persisting stable orbits. In the same figure, the 3D plot of the phase space highlights the Poincaré section plane $\dot{C}_L = 0$, $\ddot{C}_L < 0$. The intersection points, shown in the frame bottom-right, represent the locus of maxima (here clustered in one point only).

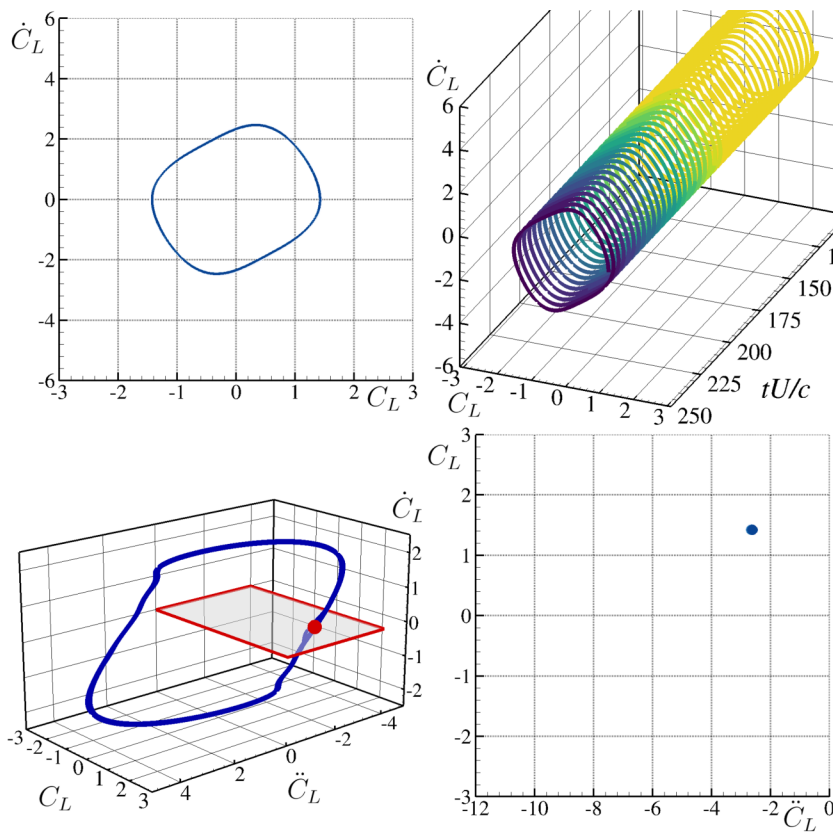


FIG. 5. Phase map (top-left) and Poincaré section (bottom-right) for $Re = 1000$ case. The 3D plot of the phase map with the time axis is depicted top-right. The phase space is drawn bottom-left. The phase map lines, as well as the Poincaré section dots, are contoured darker blue with time.

IV. MODULATING CASES: $Re = 2000, 3000$

By increasing the Reynolds number, a low-frequency modulation in the lift signal appears and the wake dipoles start to strongly interact. The wakefields for $Re = 2000$ and 3000 are depicted in Fig. 6, where the dipoles shed in the wake are clearly distinguishable, as well as their mutual interaction for $x/c > 16$ at $Re = 2000$ and $x/c > 11$ at $Re = 3000$, respectively. For $Re = 3000$ a thinner filamentation is visible during the formation of the first shed dipole. When the vortex patches in the wakefield are arranged in a double row fashion, a stability analysis is needed, as performed by Kurtulus [36], or Birkhoff [37] and recently Jiang and Cheng [17], where the ratio between the vertical and horizontal distances of the vortices plays the role of a key parameter. Although for low Reynolds numbers (~ 100) this approach is reasonable because of the wake configuration, where there are two rows of counter-rotating vortical structures continuously shed in the flow field, in the present Reynolds number range this investigation approach may be meaningless. Kurtulus [36] tried such an approach for the flow past a NACA0012 profile at $Re = 1000$, when the angle of attack varied from 0° to 90° , but the slim shape of the profile is more suitable for triggering the vortical wake separation in two rows of vortices, at least for low incidences. Since the cylinder is a blunt body, the vortices interaction in the wake is more intense so the arrangement in two vortex rows is rapidly lost when the Reynolds number increases. At $Re = 1000$ this analysis leads to a very low ratio between the transverse distance between vortex rows and the longitudinal separation

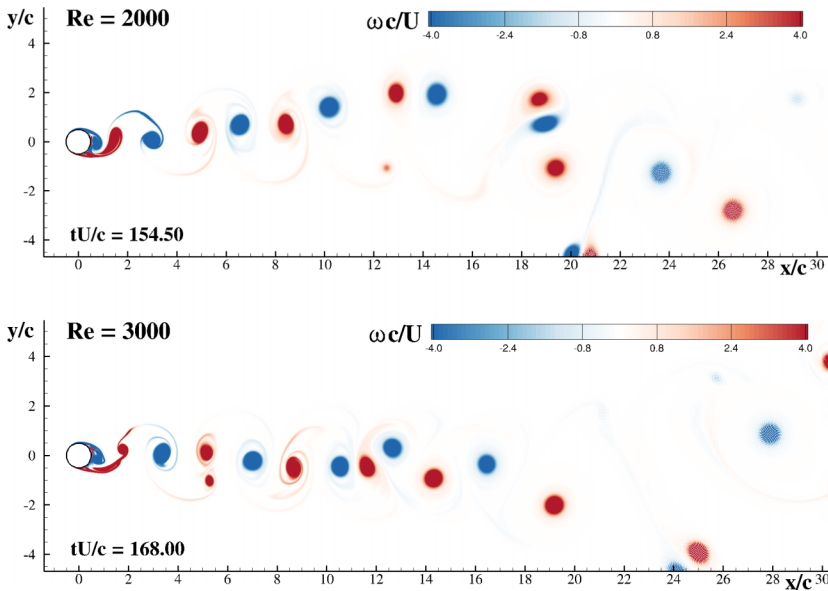


FIG. 6. Cylinder vorticity wake for at maximum lift. Top $Re = 2000$, bottom $Re = 3000$, see Supplemental Material [44].

between vortex patches of the same circulation (h/l according with the definition of Kurtulus [36]), since the dipoles are practically aligned. Conversely, for the cases of the present section, the wake is not stable at all, having a continuous drift upward and downward similarly to the wake oscillator model investigated in the eighties by Tamura and Matsui [38]. In that pioneering work, a simple mass-spring simplified approach, the wake length variation due to the vortex shedding was able to predict the shedding frequency with surprising accuracy (i.e., $tU/c = 0.2$). In Fig. 7 the oscillation

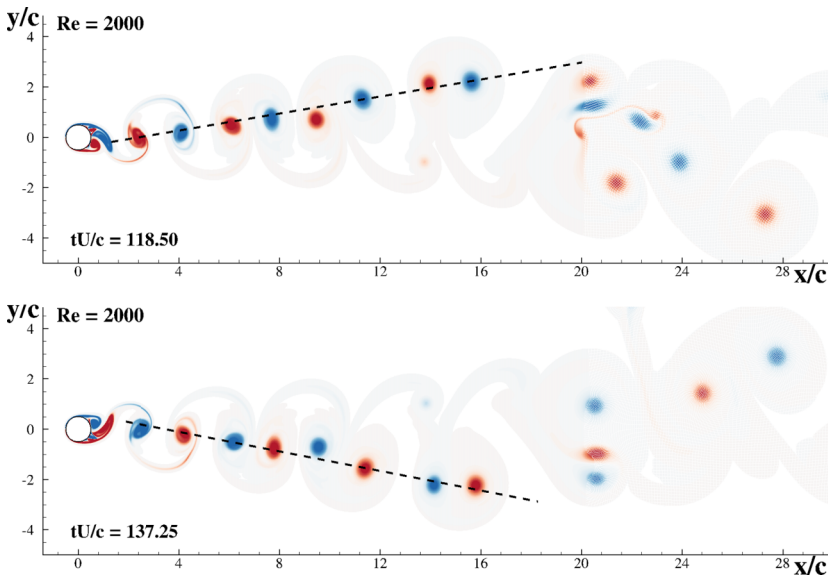


FIG. 7. Cylinder vorticity wake modulation at $Re = 2000$.

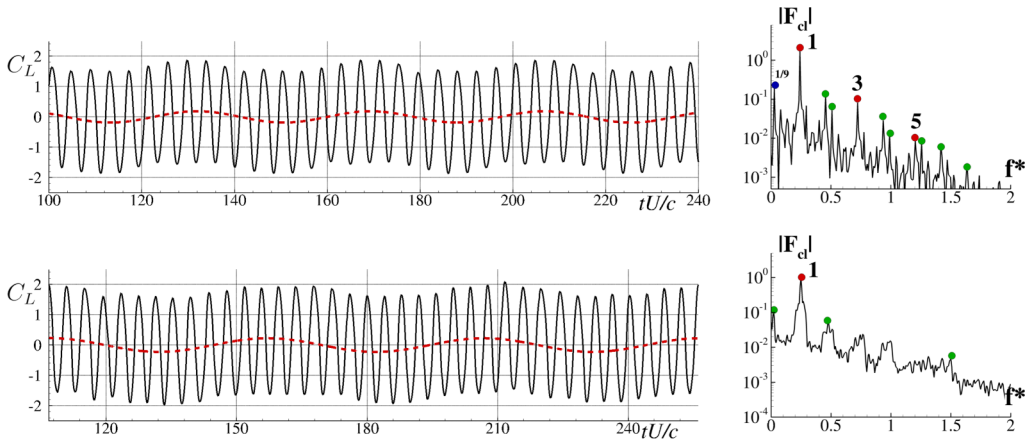


FIG. 8. Lift time signal at regime conditions and corresponding Fourier analysis for $Re = 2000$ (top) and $Re = 3000$ (bottom) cases. The low frequency modulation is superimposed with a dash line.

of the wake is highlighted for $Re = 2000$, by drawing the lines connecting the vortex patches. This oscillation takes place at a frequency significantly lower than the shedding one, so that a low frequency modulation is expected. In Fig. 8, the lift time signals for $Re = 2000$ and $Re = 3000$ cases are plotted, clearly revealing the force modulation. This latter is drawn with a dashed line and superimposed to the lift signal.

In the Fourier transforms, reported in the side plots, the modulating frequency is around 0.0267 for $Re = 2000$ and 0.02 for $Re = 3000$, so that the periods of the modulations are 37.5 and 50, respectively. This analysis indicates that the modulation is more persistent for increasing Reynolds number, although its amplitude tends to decrease from 0.37 to 0.22 in the present example. The discrete peak arrangement of the spectrum still visible in the $Re = 2000$ case is almost lost in $Re = 3000$: this means that the force time signal, although periodic at first sight, is actually evolving toward a nonperiodic condition. The peaks at the odd harmonics, similarly to the $Re = 1000$ case, are found for $Re = 2000$ and highlighted with red circles in the top-right frame of Fig. 8. The modulation is related to the subharmonics $1/9$, highlighted with a blue circle, whereas the other peaks of the spectrum are placed at irrational multiples of the main frequency (green circles). To assess the reliability of the present analysis, a comparison with a finite volume method solution is given in Appendix B.

For $Re = 3000$, there are only irrational peak frequency multiples. The frequency of the carrier signal remains quite constant, slightly increasing from 0.240 in the $Re = 2000$ case to 0.248 at $Re = 3000$.

The autocorrelation functions, shown in Fig. 9, are very similar to the $Re = 1000$ case, revealing again highly correlated signals. The longer period of the modulation at $Re = 3000$ makes the signal slightly less correlated for large time lags, as is visible in the same figure. The power spectral density shows a single peak corresponding to the frequency of the carrier signals, similarly to the $Re = 1000$ case discussed before. The presence of the modulation is reflected in a scattering of the force orbits in the phase maps in the left frames of Fig. 10. The thickness of the strips in which the orbits scatter is directly related to the intensity of the modulation, appearing thicker for the $Re = 3000$ case.

The orbits exhibited by the lift time signals can be interpreted as a condition that is still far from a chaotic transition, where the map appears as a tangle of orbits (see Durante *et al.* [15]), but some remarks may be immediately made.

The orbits at $Re = 2000$ are almost regular and well described through simple convex curves. The Poincaré section coherently shows a group of clustered points, weakly scattered due to the presence of the modulation. Conversely, at $Re = 3000$, the situation is more severe: the orbits wiggle more

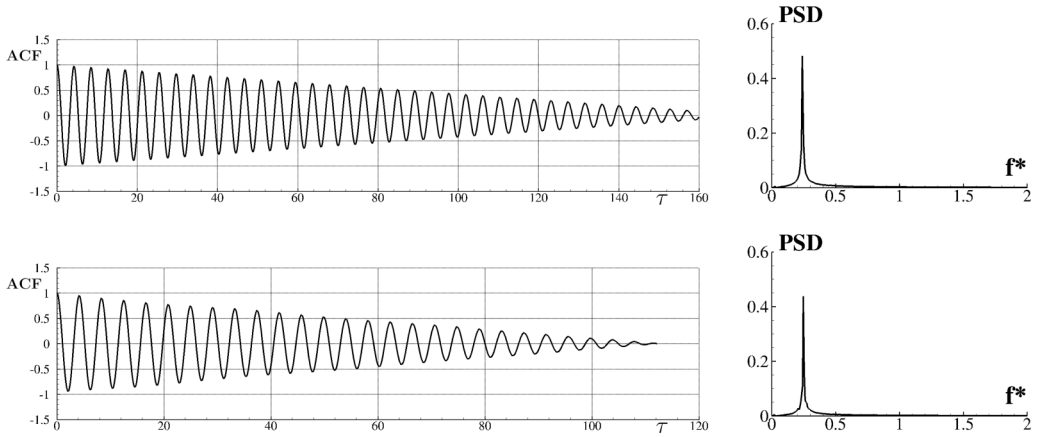


FIG. 9. Autocorrelation functions for $Re = 2000$ (top) and $Re = 3000$ (bottom) cases and corresponding PSD. With τ the nondimensional time lag of the signal is indicated.

during the time evolution because of the change in the concavity of the lift signal. This effect is more evident in the Poincaré section (drawn on the right), where the group of points corresponding to the lift maxima are more spread along the \dot{C}_L axis, but less over the C_L one. This is caused by a frequency modulation of the time signal; indeed, from the Fourier spectra depicted in Fig. 8 at $Re = 3000$ the spectrum does not present sharp peaks unlike the $Re = 2000$ case.

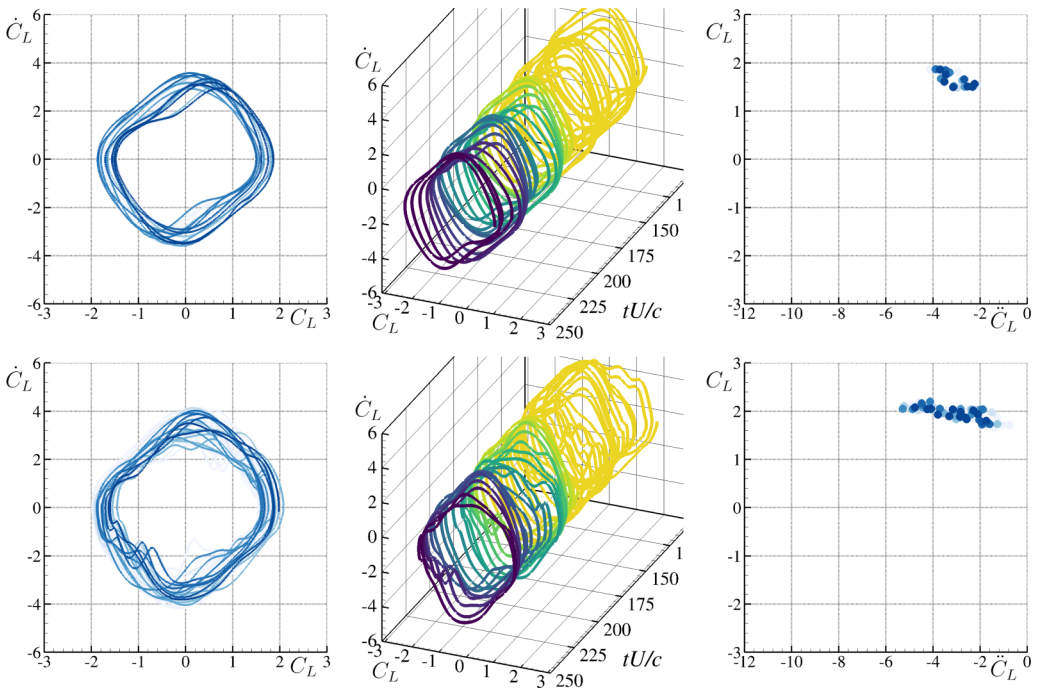


FIG. 10. Phase map (left), 3D view of the map (center) and Poincaré section (right) for $Re = 2000$ (top) and $Re = 3000$ (bottom) cases. The phase map lines, as well as the Poincaré section dots, are contoured darker blue with time.

From the connection between the force on the body and the wake topology, as explained in Graziani and Bassanini [21] and Riccardi and Durante [39], the lift is related to the vorticity field according to the relation

$$L(t) = \rho \int_{\Omega} dx x \frac{\partial \omega(x, t)}{\partial t}, \quad (6)$$

where Ω is the fluid domain.

The relation Eq. (6) is founded on a Eulerian description of the flow field where the lift force is related to the time derivative of the vorticity field first moment. In a Lagrangian fashion, a singular distribution of the vorticity related to the vortex particle method is considered, so that Eq. (6) becomes

$$L(t) = \rho \frac{d}{dt} \left(\sum_{j=1}^{N_v(t)} x_j(t) \Gamma_j(t) \right), \quad (7)$$

where x_j and Γ_j are, respectively, the horizontal position and the circulation of the j th vortex particle among the N_v vortices at time t . It is worth noting that the vortex particle number changes with time [i.e., $N_v = N_v(t)$], because the vortices are created on the body surface at each time step and redistributed over a regular mesh during the diffusion step. The increasing complexity of the vorticity field, coming from the filamentation and subsequent mutual interaction, influences the vorticity time variation. In fact the departure of the lift time signal from a regular periodic behavior mainly depends on the vortex interaction, as highlighted by the phase maps and Poincaré sections shown above.

V. CHAOTIC TRANSITION WITH INTERMITTENCY: $Re = 3100-4000$

When the Reynolds number exceeds 3000, the shedding mechanism becomes more and more complicated, as discussed also in Durante *et al.* [14], with large vortex structures forming complex wake patterns. From $Re = 3100$ to $Re = 4000$ the force time signal shows intermittent irregular patterns that depend on mutations in the shedding mechanism, or on new arrangements of the near/medium wake.

A. Case $Re = 3100$

Starting from the lowest Reynolds number case, Fig. 11 depicts the lift time signal, its Fourier spectrum and some frames of the shedding mechanism. Despite the small increase in the Reynolds number, compared to the $Re = 3000$ case previously discussed, the lift appears rather erratic with significant amplitude and frequency modulations, without exhibiting a clear pattern of recurrence during time evolution.

The shedding frequency, after the increase recorded from $Re = 1000$ to 3000 (0.235 to 0.248), decreases to $f^* = 0.24$. The spectrum is almost continuous without any pronounced peak except at the shedding frequency. In spite of that, a small peak is found at $f^* = 0.12$, revealing a persisting modulation at half of the carrier frequency.

In the upper frames of Fig. 11, different shedding mechanisms observed in the present case are highlighted and referred to with the corresponding number. In the transient range (not shown in the lower frame), where the stream velocity increases, the upper and lower shear layers undergo an intense roll up that finally leads to the formation of two counter rotating vortex patches. As usually observed, the vortices remain in a stable configuration for a while, then they become unstable and the onset of the shedding phase takes place. The interaction between the wrapped layers induces an intense strain which alternatively leads to the detachment of vorticity. It is observed that the interaction can manifest with the formation of vortex filaments (frames 2 and 3) or with the elongation and the 90° bending of the wrapped shear layer (frames 4 and 5). More interesting is the unexpected pause time range, to the authors' knowledge never documented, where the shear

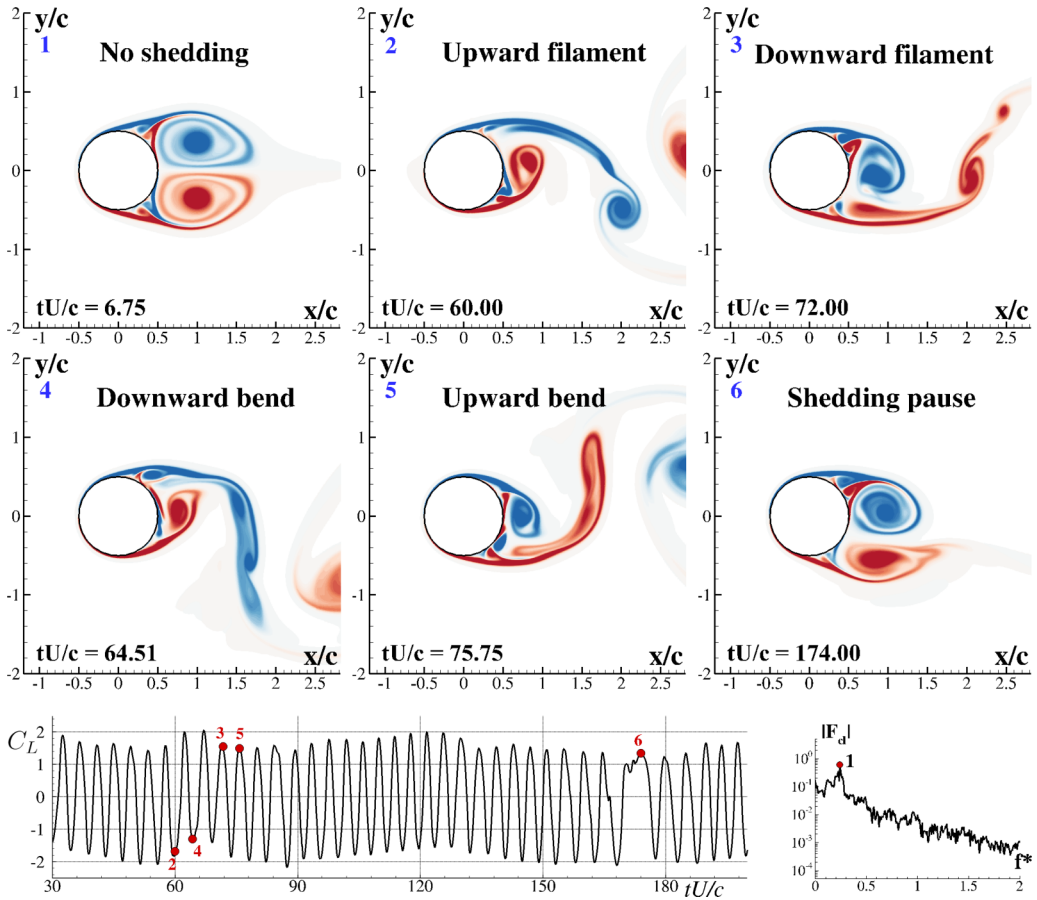


FIG. 11. Different shedding mechanisms observed at $Re = 3100$ referenced with the corresponding number in vorticity fields. Top: vorticity fields at different nondimensional times. Bottom: lift time signal and corresponding Fourier spectrum; with red dots the shedding time instants depicted on top frames and indicated with the corresponding number.

layers are arranged in a stable configuration without shedding. This condition is depicted in frame 6 of Fig. 11 and better highlighted in Fig. 12, where two time instants within the pause range are depicted. When the pause appears, the wrapped shear layers form two stable counter rotating vortices and the near dipoles depart from the cylinder. In the bottom frame of Fig. 12, the same condition is illustrated in terms of force time signals. The lift remains almost constant, although there is a slight increase caused by the downward arrangement of the layers, whereas the drag, on the contrary, decreases by about 43%.

In Fig. 13 the phase maps related to different time ranges are depicted and the corresponding ranges are delimited with vertical lines in the top frame of the same figure. These time ranges were identified through a wavelet transform, as described in Appendix C. The autocorrelation function and the related PSD are depicted in Fig. 14. The left frame shows that the signal loses correlation with increasing time lag, recovering a weakly correlated condition (the function amplifies) when the lag exceeds a duration of $tU/c = 170$, thus indicating that the irregular intermittency strongly decorrelates the signal. For higher Reynolds numbers, the autocorrelations are shown and discussed in Appendix A. The regularity of the different intervals is also reflected on the phase maps and Poincaré section arrangements. The latter are drawn in Fig. 15. To improve clarity, the whole set of

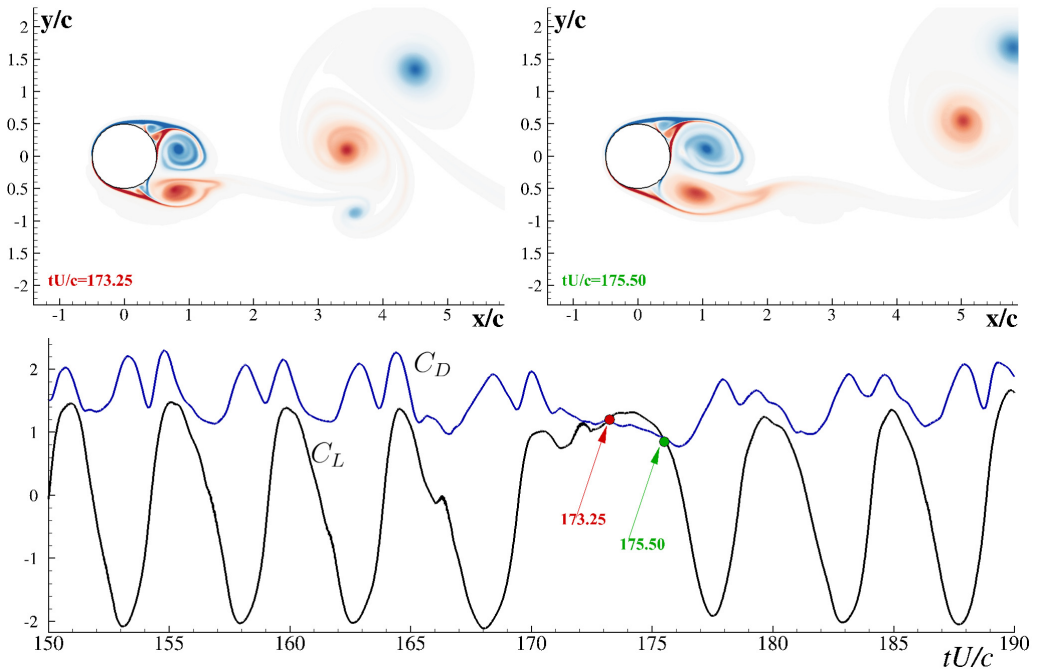


FIG. 12. Example of the shedding pause at $Re = 3100$. Top: the vorticity fields; bottom: the lift (black solid) and drag (blue solid) time signals.

signal maxima is indicated with small green diamonds. The black circles indicate the subset falling within the regular time range, whereas red triangles are used for the irregular ranges.

In frame 1, the interval $tU/c \in [36.6, 59.06]$ is considered. The map shows numerous orbits, where the final two (wider) are almost superimposed, thus indicating a periodic behavior. In the second frame, two groups of orbits behave as in a doubling-period bifurcation. This means that the system has not yet reached a stable configuration. This can be also deduced from Fig. 16, where the top frame refers to the nondimensional instant $tU/c = 75.75$. The wake is evidently widely extended, with dipoles shed upwards and downwards, thus affecting the irregularity of the corresponding phase orbits. In this case, the 90° bending of the wrapped shear layers is visible. Frame 1 of the Poincaré sections depicted in Fig. 15 shows a group of points only slightly scattered along the \dot{C}_L direction, thus showing the lack of a stable orbit and a small variation in terms of concavity of the force time signal.

Frame 3 refers to the time interval $[93.35, 121.58]$ where the solution exhibits almost regular orbits slightly scattered because of the lift modulation, visible in the force time signal shown in the top frame. This is also reflected in the compactness of the vorticity wake visible in the middle frame of Fig. 16. As it can be deduced from frame 3 in Fig. 15, in addition to the lift variation in terms of peak modulation, a concavity variation is also present so that the lift maxima are rather spread horizontally.

In frame 4, the shedding pause appears. The phase map related to this time interval shows intricate orbits with numerous knots indicating an unstable condition which ends with the pause event. Similarly, the Poincaré section spreads out along the C_L axis, which is the typical behavior of the inception of a chaotic transition (see also Durante *et al.* [16]).

The situation changes again during the next time range, depicted by the phase map in frame 5, where a stronger stability is regained. The time signal appears more regular and the orbits are almost clustered. The set of points of the related Poincaré section (frame 5 of Fig. 15) is dually bunched in a

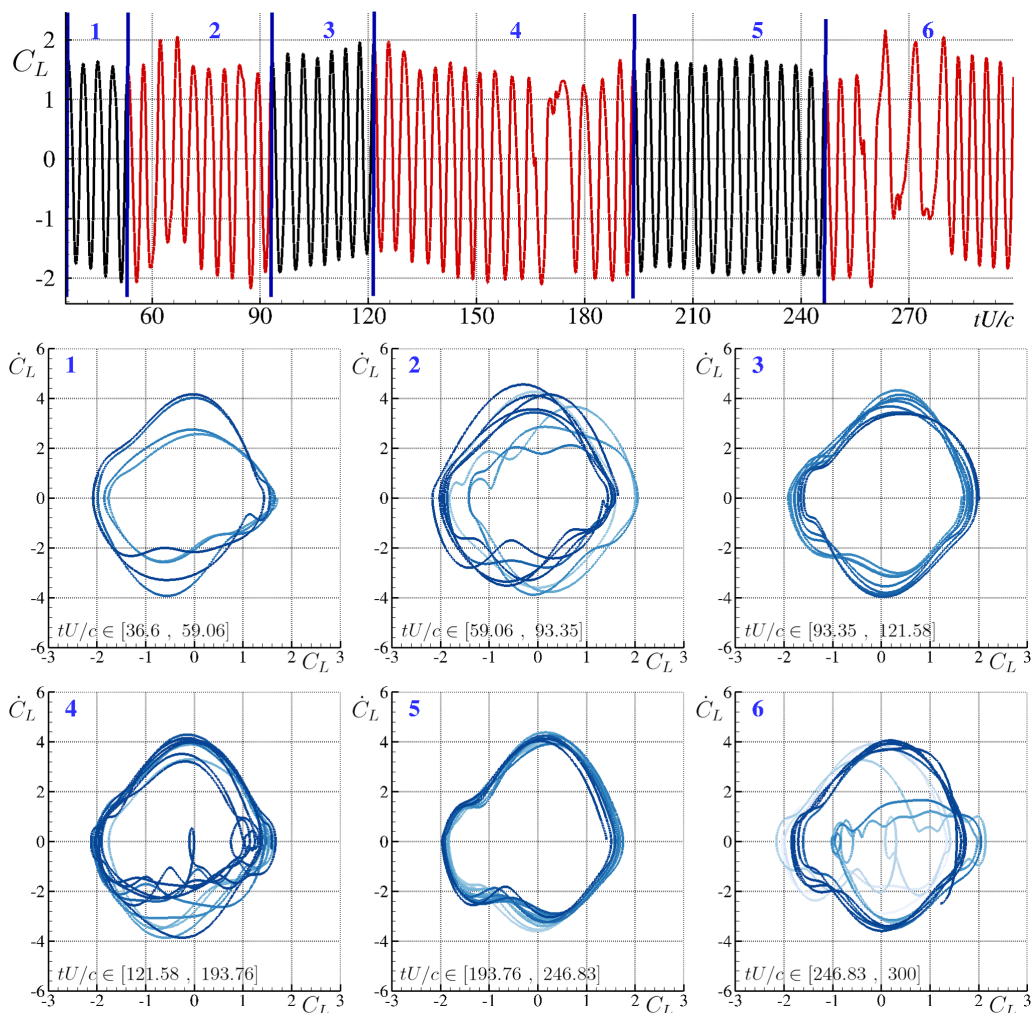


FIG. 13. Phase maps for different time ranges at $\text{Re} = 3100$. Top: the lift time signal; the time ranges considered (delimited with solid lines) are highlighted. Bottom: the corresponding maps. For the sake of readability, the frames are numbered and the same numbers are indicated at the corresponding time range. The maps are contoured darker with time (the contour ranges are adapted to the corresponding interval).

small area. Furthermore, the associated shedding (bottom frame of Fig. 16) induces the development of a rather compact wake field.

In the last time interval investigated, a new instability appears with a double orbit phase map (frame 6 of Fig. 13). Three higher peaks in the lift time signal (range 6), distanced by a wider period, are responsible for the tight inner orbits found in the map. The Poincaré section appears completely spread out, resembling a chaotic condition.

When the irregularity becomes more pronounced, the Fourier spectrum moves toward a continuous arrangement, thus not permitting a clear identification of the shedding frequency. The PSD allows one to isolate the frequency at which the power of the signal presents a peak, making it possible to find the desired frequency. Obviously, as observed in Figs. 4 and 9, when the signal is periodic and the Fourier spectrum is peak-shaped, the frequency associated to the highest amplitude is equal to the corresponding power spectrum peak. In the present case, as shown in the right frame

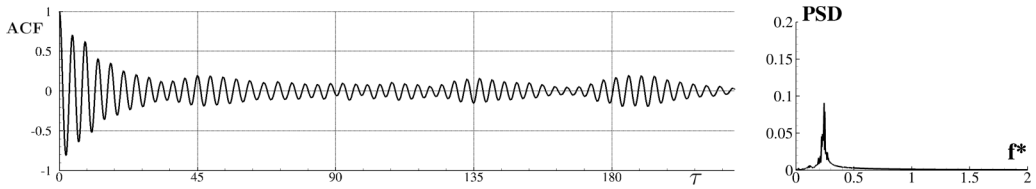


FIG. 14. Autocorrelation function (on the left frame) and power spectral density (on the right frame) for the case $Re = 3100$. With τ the nondimensional time lag of the signal is indicated.

of Fig. 14, a single spectrum peak is visible at $fc/U \simeq 0.25$ whereas the Fourier spectrum shows two peaks at 0.24 and 0.12, as stressed above. For higher Reynolds numbers, the situation becomes more intricate and the two frequencies may differ significantly. At $Re = 8000$, for example, a Fourier peak is absent, whereas a PSD peak is clearly evident at 0.17.

In general, we can conclude that in this case, although a general regular pattern in the force time behaviour cannot be found, a transition toward an irregular condition is experienced but a chaotic condition is not attained. From the erratic intermittency of the irregular ranges, it is reasonable to assume that a regime condition, where these instabilities are no longer present, never appears.

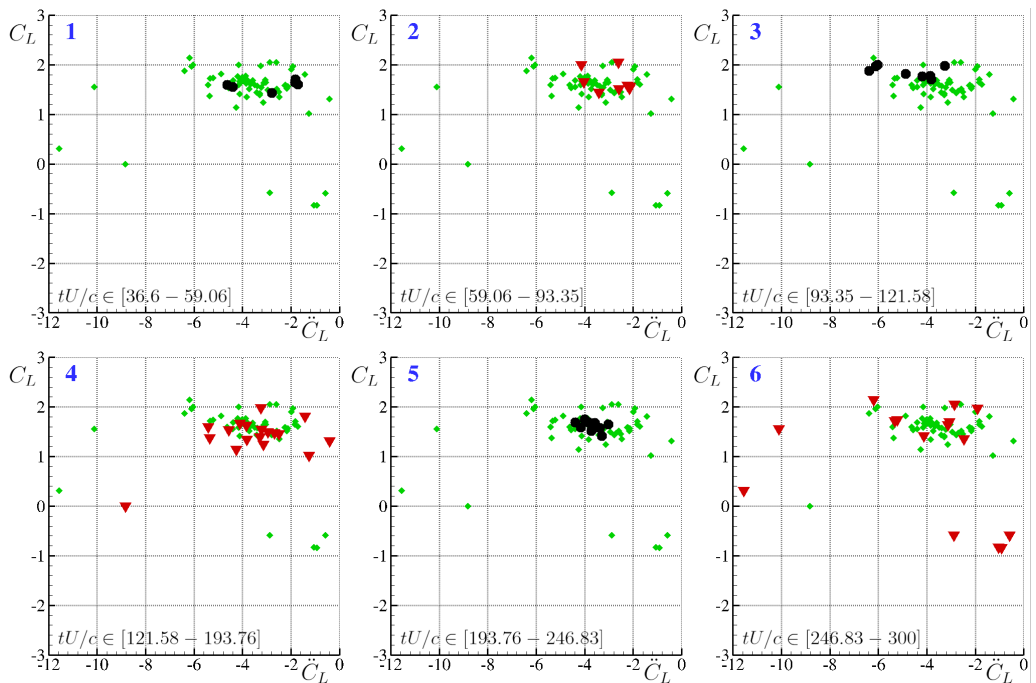


FIG. 15. Poincaré sections for different time ranges at $Re = 3100$. Small green diamonds: the full set of maxima; black circles: the maxima of the periodic time ranges; red triangles: the maxima of the irregular ones. For the sake of readability, the frames are numbered and the same numbers are indicated in the corresponding time range.

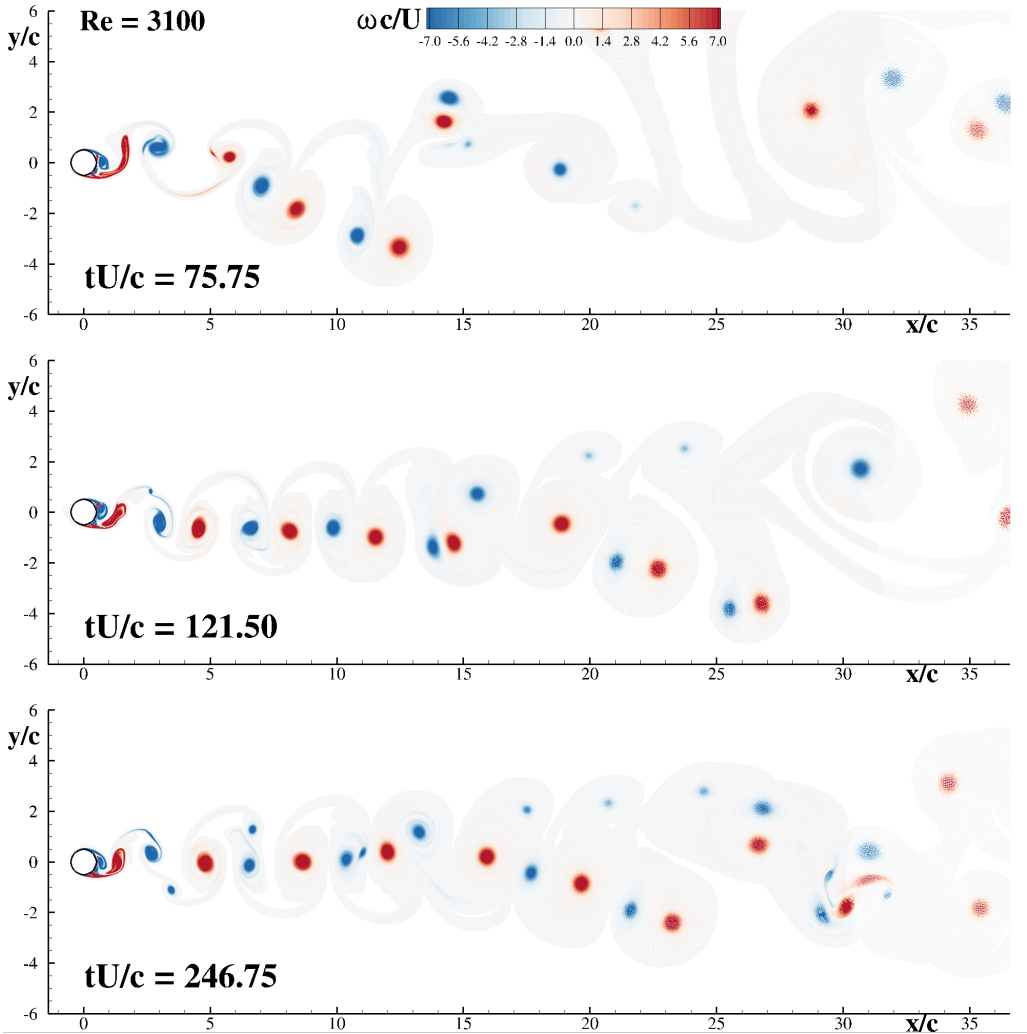


FIG. 16. Vorticity far field for time instants falling in ranges 2, 3, and 5 of Fig. 13.

B. Cases $Re = 3200\text{--}4000$

In the present section, the Reynolds range 3200–4000 is investigated. Some points and methodologies of the previous subsection are here reiterated. As pointed out above, intermittency in the lift time behavior is observed numerous times during the evolution considered. This also occurs in the present range, where the system moves back and forth between regular and irregular behaviours. Figures 17 and 18 show the time histories of the present cases, with the separation of the different ranges by vertical solid lines. To better grasp the different trends, Fig. 19 depicts the corresponding Poincaré sections evaluated for each case. As evidenced, the black circles are the maxima of the periodic time ranges, whereas the red triangles are the corresponding maxima of the irregular ranges.

It should be stressed that the black circles are more clustered when a modulating term is weak or absent. In this case the section appears to be similar to the right frame of Fig. 5 for no modulation (i.e., $Re = 1000$), or to the right frame in the top row of Fig. 10 for weak modulation. In the case of severe modulation, the lift maxima are more scattered horizontally if the modulation affects

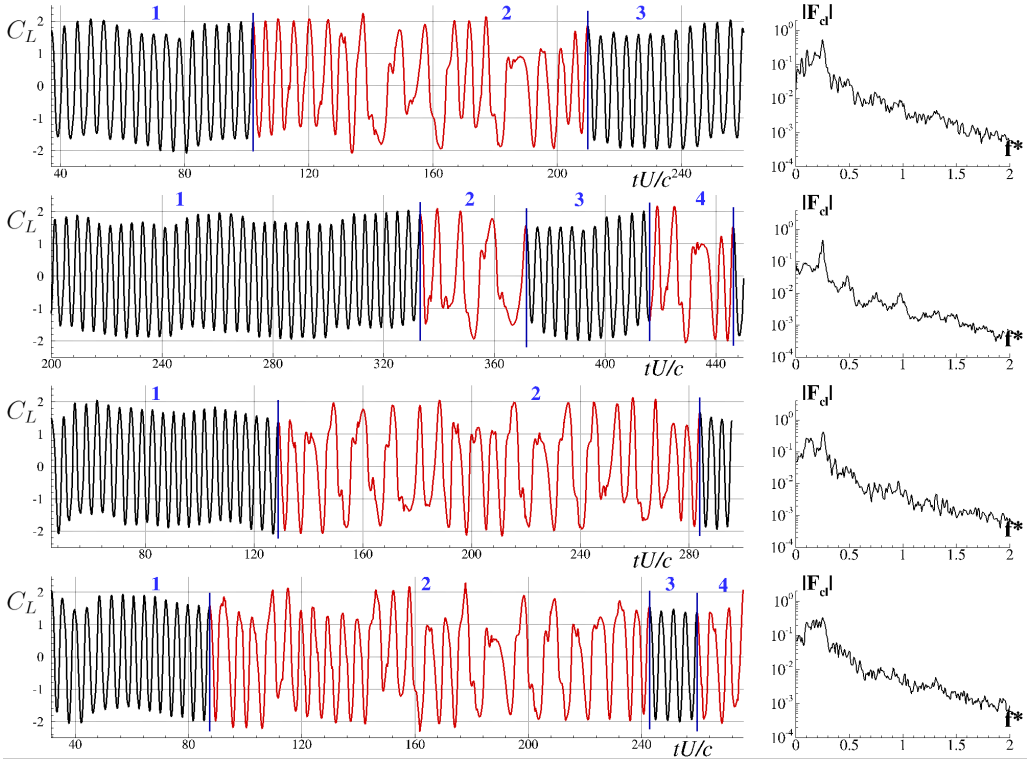


FIG. 17. From top to bottom: lift time signals and Fourier spectra for Reynolds numbers from 3200 (top) to 3500 (bottom). Different time ranges where specific behaviours are found are separated with vertical solid lines. The irregular time ranges are highlighted in red.

the concavity (e.g., FM: frequency modulation as shown in the right bottom frame of Fig. 10 for $Re = 3000$) and vertically if it affects the amplitude (e.g., AM: amplitude modulation). If we refer to the lift time signals, it can be immediately deduced that the irregular ranges incept without any predictable scheme and do not follow a straight route as the Reynolds number increases, as seen in the case of elliptic profiles, investigated in Durante *et al.* [15]. Conversely, more information is conveyed by the Poincaré sections in Fig. 19. Generally, the periodic ranges show a weak vertical scattering of maxima with respect to the nonperiodic ones. However, for $Re = 3300$ and $Re = 3800$ the lift maxima are tightly clustered horizontally as well, thus indicating a limited frequency modulation of the signal during the periodic ranges (labeled 1 and 4, respectively). For these cases, the periodic ranges of the signal are more similar to a genuine periodic signal. Significantly wider horizontal dispersion in the periodic range is found in the cases 3500, 3700, 3900, and 4000, thus indicating a frequency modulation.

With red symbols in the same figure, the maxima related to irregular ranges show a wide dispersion in both directions. This is due to the presence of local sparse maxima related to spurious irregular oscillations. The quantity and the scattering of these points varies not-monotonically with the Reynolds number.

To quantify the departure of the dynamical system from a regular periodic condition, the ratio between the number of irregular maxima N_{irr} over the total maxima N_{Tot} was evaluated and is depicted in Fig. 20, where the density $\rho_{irr} = N_{irr}/N_{Tot}$ is shown. This frame highlights that the number of irregular maxima decreases for $Re = 3300$ and $Re = 3800$, as previously observed. It is worth noting the decrease observed in the range 3600–3800 after which a new increase appears,

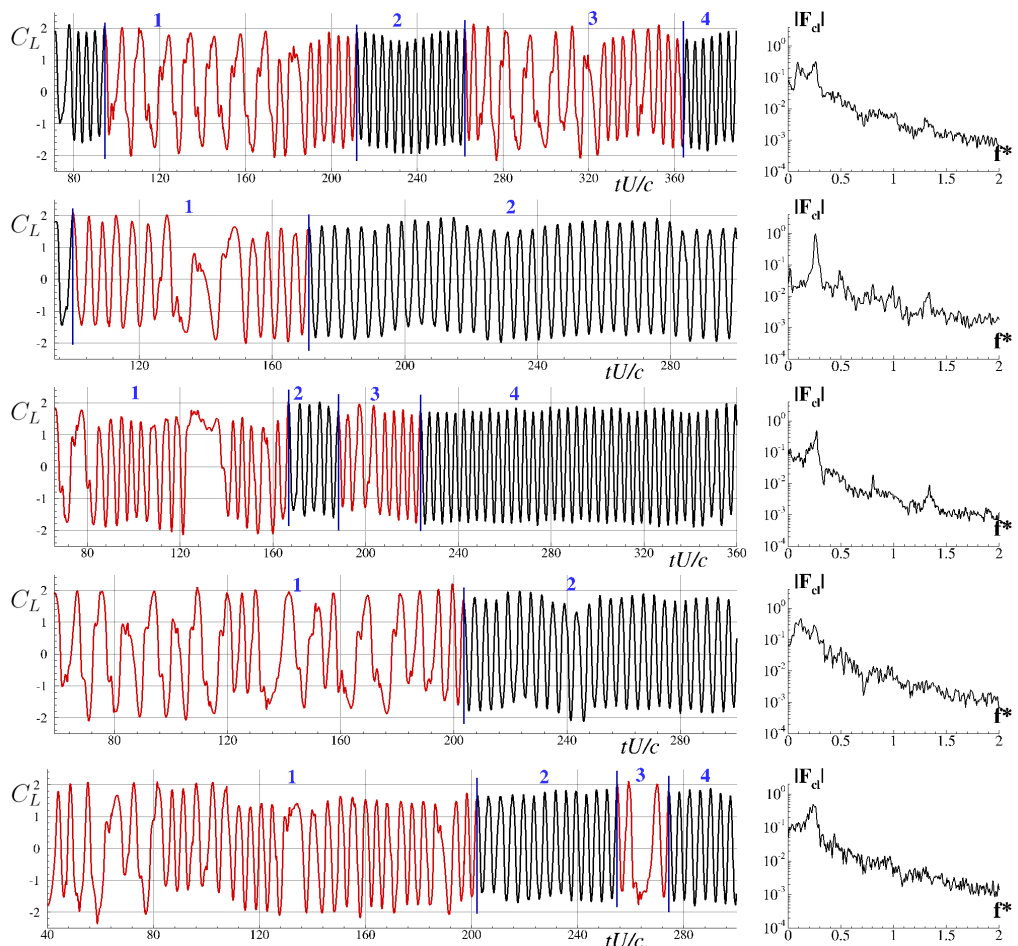


FIG. 18. From top to bottom: lift time signals and Fourier spectra for Reynolds numbers from 3600 (top) to 4000 (bottom). Different time ranges where specific behaviours are found are separated with vertical solid lines. The irregular time ranges are highlighted in red.

indicating that there is not a straight route toward a chaotic condition, as also found in Durante *et al.* [16] for the flow past a NACA profile at varying angles of attack.

VI. CHAOTIC BEHAVIOR: $Re = 5000\text{--}10\,000$

The range going from $Re = 5000$ to $10\,000$ is characterized by a chaotic behavior. As shown on Fig. 21, the periodic ranges are almost absent in these cases, although a short one is found for $Re = 6000$. The Fourier spectra still show an amplitude area for $f^* \approx 0.18$ for all cases but $Re = 6000$, where $f^* \approx 0.22$, thus revealing that the shedding mechanism presents a dominant frequency anyway. It must be stressed that the regular ranges are identified through the phase maps, when the orbits are regular closed curves and the related Poincaré sections show almost clustered points. For the present cases, this procedure identifies one range only for $Re = 6000$, evidenced in the corresponding frame of Fig. 21. The related Poincaré sections are depicted in Fig. 22 for all the Reynolds number cases investigated. It is worth stressing that the irregular behavior of the lift time signal is also associated to the presence of local maxima for negative values of the force. While for $Re = 5000$ and 6000 , the positive and negative C_L maxima are rather separated

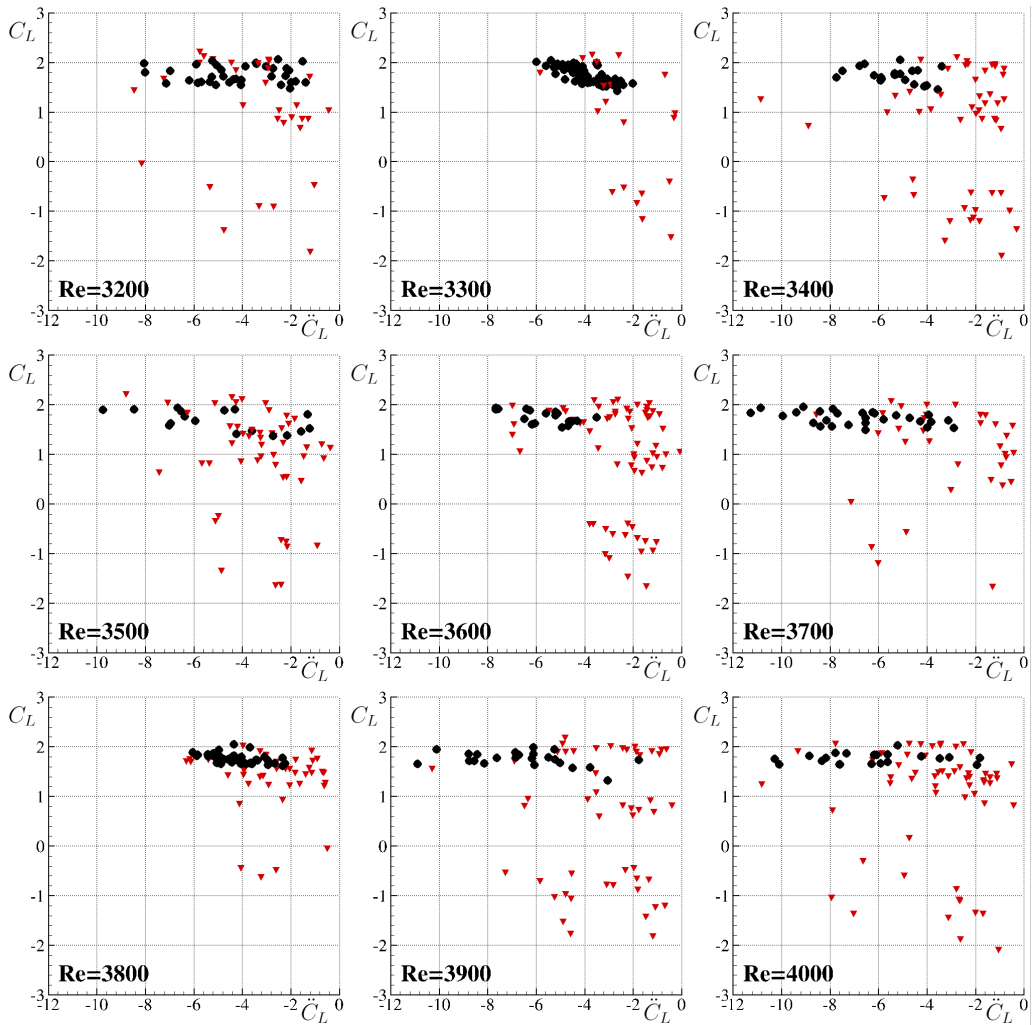


FIG. 19. Poincaré sections for Reynolds numbers spanning from 3200 to 4000. Maxima related to regular time ranges are represented with circles, irregular time ranges with red triangles.

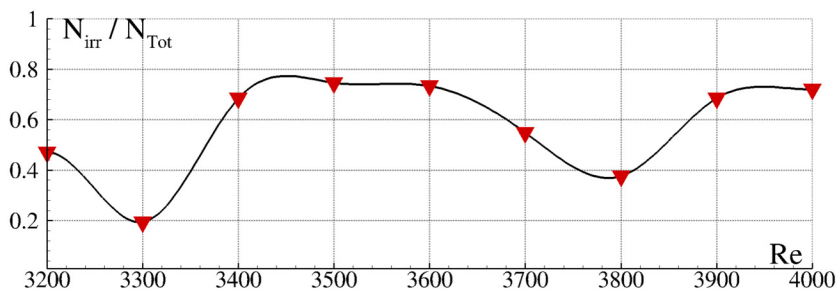


FIG. 20. Ratio between irregular number of maxima over the total maxima for Reynolds numbers ranging from 3200 to 4000.

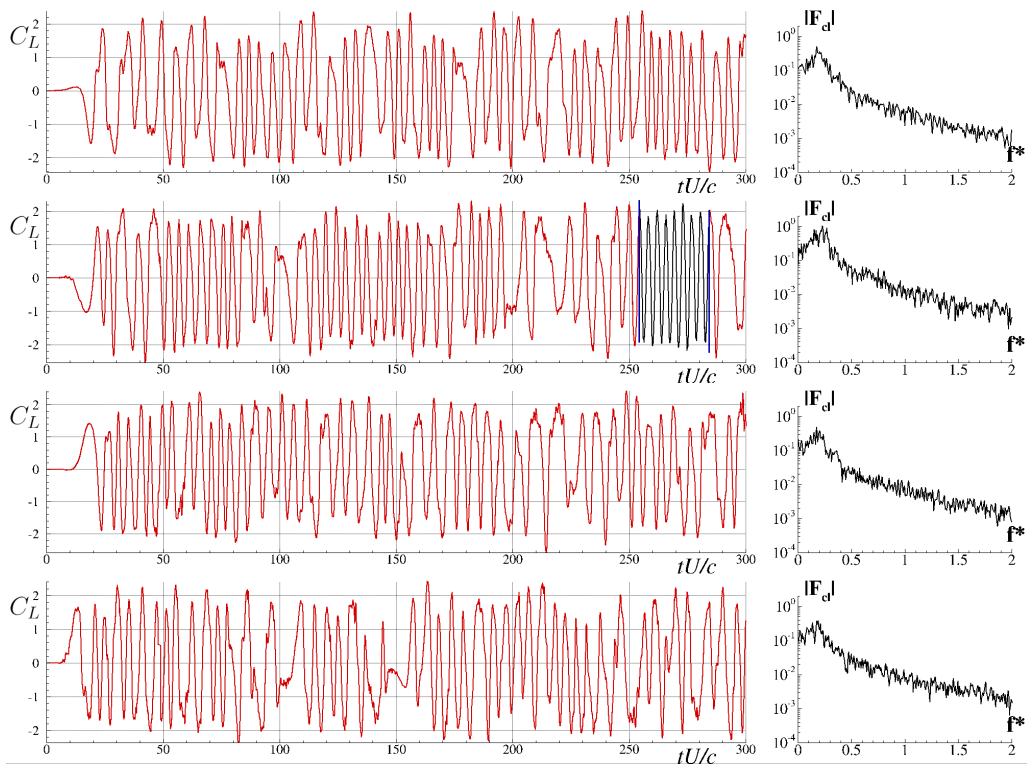


FIG. 21. From top to bottom: lift time signals and Fourier spectra for different Reynolds numbers. From (top): 5000, 6000, 8000, 10 000 (bottom). The cases $Re = 7000$ and $Re = 9000$ were investigated but are not shown for the sake of readability. The irregular time ranges are highlighted in red.

in two distinguishable clusters, for higher Reynolds numbers this distinction disappears and the section points are more and more homogeneously scattered over the Poincaré plane. The presence of two groups of maxima, also found for $Re = 3300$ and $Re = 3600$, suggests that the irregular ranges are the mark of some instability that incepts when the shear layers (upper when lift is minimum, lower when maximum) are detaching from the cylinder. Conversely, as discussed in Durante *et al.* [14], at higher Reynolds numbers the effect of local strain makes the shear layers so thin and their interaction so complex that already in the near wake the vorticity is shed over a large spectrum of scales (see Fig. 11 of Ref. [14]). This behavior implies that the shedding becomes so chaotic that the force time signal follows the same route. Thanks to Eqs. (6) and (7), it can also be remarked that the chaotic behavior of the force time signal is the reflection not only of the near wake dynamics, but of the whole vorticity field. In fact, as remarked in Sec. III, the lift force depends on the time derivative of the first moment of the vorticity, which is represented as an integral extended to the unbound set Ω .

A clear representation of the chaotic nature of the vorticity field at the highest Reynolds number is given in Fig. 23, where the near and far wakes are depicted. As discussed in Durante *et al.* [14], although the presence of a large number of vortex scales appears in the flow field without any regular shedding, the inverse cascade typical of a two-dimensional vorticity field rearranges the wake in large dipoles, clearly visible in the left frame of Fig. 23.

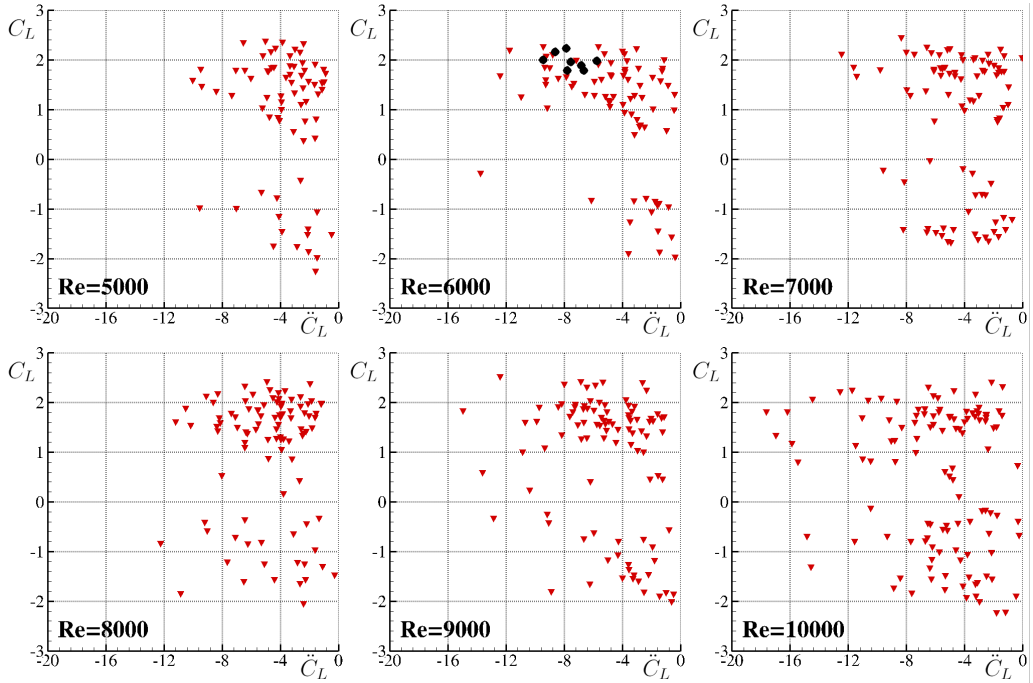


FIG. 22. Poincaré sections for Reynolds number spanning from 5000 to 10 000. Maxima related to regular time ranges are represented with circles, irregular time ranges with red triangles.

VII. OVERALL CONSIDERATIONS

In the present section some overall considerations are addressed. To evaluate the chaotic transition of the dynamical system, it is worth commenting on the maximum Lyapunov exponent drawn in Fig. 24. From the pioneering work of Wolf *et al.* [40], given a continuous dynamical system in an n -dimensional phase space, the long-term evolution of an infinitesimal n -sphere of initial conditions is considered; the sphere becomes an n -ellipsoid for the locally deforming nature of the flow. The i -th Lyapunov exponent is then defined in terms of the length of the ellipsoidal principal axis $p_i(t)$:

$$\lambda_i = \lim_{t \rightarrow \infty} \frac{1}{t} \log_2 \frac{p_i(t)}{p_i(0)},$$

where this axis may expand or contract, thus corresponding to positive or negative exponents.

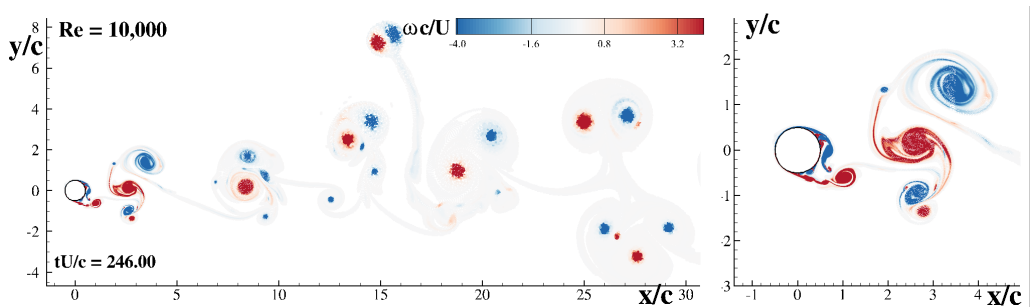


FIG. 23. Vorticity field for $Re = 10\,000$. The left frame depicts the far field at maximum lift, while the right frame is a magnification of the near wake, see Supplemental Material [44].

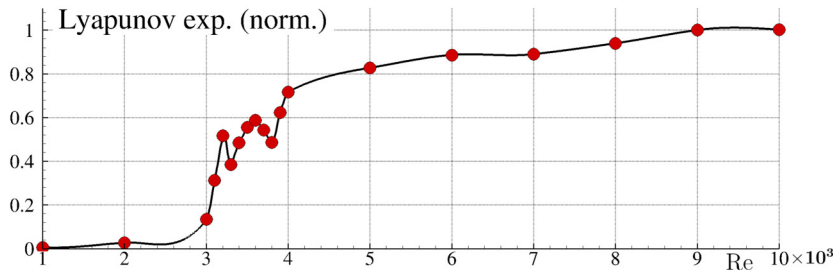


FIG. 24. Maximum Lyapunov exponents distribution for all the Reynolds numbers investigated. The exponents are normalised with respect to the maximum value.

Each positive exponent reflects a “direction” along which the system experiences the repeated stretching and folding that decorrelates the nearby states on the attractor. When the behavior of the dynamical system is highly sensitive to the uncertainties on the initial conditions, its long-time behavior cannot be predicted: this is chaos.

The sign of the Lyapunov exponent provides a qualitative picture of a system dynamics: positive values are related to systems going toward chaotic conditions, negative or zero values are related to stable systems.

In the present work, the Wolf algorithm was applied to evaluate the Lyapunov exponent related to the lift time signal for every Reynolds number investigated.

As remarked by Wolf himself, a time series that appears erratic might be chaotic, or it might be multiply periodic, periodic with “noise,” or some form of pure noise. A defining feature of chaos is that small changes in the state of a system will grow at an exponential rate. The larger the positive exponent, the more chaotic the system; that is, the shorter the time scale of system predictability. A system may possess any number of Lyapunov exponents, but for it to be declared as in chaos regime we only need to confirm that the dominant (largest, or most positive) exponent is positive. Hence, it is particularly important to estimate the dominant exponent. The Wolf algorithm is able to calculate the maximum exponent, so that, if a system exhibits periodic behavior, the corresponding value will be zero or near zero, neglecting negative values. Together with the work of Wolf *et al.* [40], the algorithm and a user guide were released. Some tips were offered, one of them was that the code is very sensitive to some parameters to be fixed in the calculation set-up. Therefore the exponent value must be assumed to be merely indicative so that, when a one-parameter investigation is performed, as in the present work where the Reynolds number is the only parameter considered, the focus should be on the exponents’ trend, rather than on their calculated value. The Wolf approach is based on a fixed evolution time (FET) algorithm that creates a multidimensional phase space orbit from a one-dimensional time series by the delay reconstruction and the estimation of the dominant (largest positive) Lyapunov exponent by averaging the exponential rate of divergence of short segments of the delayed reconstructed orbit.

By considering that a precise value of the exponent is meaningless, in Fig. 24 the maxima Lyapunov exponents are normalized with the largest calculated value. For $Re = 1000$ and 2000 they are near zero so that the system exhibits orbital stability or *periodicity*, as discussed in Secs. III and IV. The exponent at $Re = 3000$ is significantly greater than zero, indicating that the system is moving toward a chaotic condition. It is also revealed by the scattering observed in the corresponding Poincaré section (see Fig. 10). In the range 3000 – 4000 , as stressed in Sec. V, an increase in the Reynolds number induces a nonstraight route toward chaos with minima reached at $Re = 3300$ and $Re = 3800$, which were the same minima found for the ratio N_{irr}/N_{Tot} , shown in Fig. 20. It is worth stressing that a different strategy for measuring the level of irregularity, by calculating the ratio between irregular maxima and all the others, leads to the same trend as that

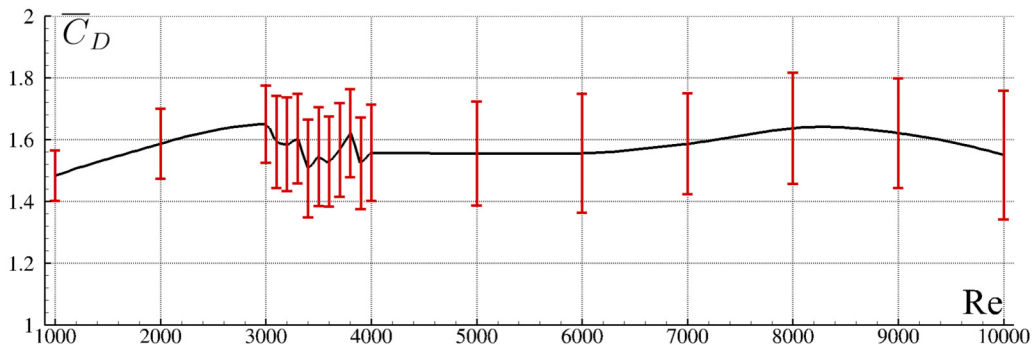


FIG. 25. Time averaged drag coefficient for the Reynolds numbers investigated. With error bars, the variance associated to every time signal.

observed with the Lyapunov exponent. An asymptotic behavior seems to be reached for higher Reynolds numbers, indicating that the chaotic condition is definitely attained.

Finally, to complete the analysis, the mean drag coefficients, together with the corresponding variance, are depicted in Fig. 25. The mean values vary slightly between 1.5 and 1.6, in agreement with Fig. 18 in Durante *et al.* [14], where the drag coefficients were calculated for Reynolds numbers spanning from 20 to 10 000 and the drag crisis mechanism was identified between $Re = 50\,000$ and $Re = 100\,000$. This work refines that calculated trend in the range 1000–10 000.

VIII. CONCLUSIONS

In the present work, the analysis of the two-dimensional flow past a circular cylinder at Reynolds numbers varying from 1000 to 10 000 was performed. The numerical code adopted in the present investigations is a vortex particle method, called diffused vortex hydrodynamics (DVH), which allows very detailed simulations and long evolution. In analogy with Durante *et al.* [16], the lift time signal was considered because of the relation between the force on the body and the vorticity field [see Eq. (6)]. From a fully periodic behavior, typical at low Reynolds numbers, the system moves toward a chaotic condition, showing irregular patterns within a periodic time signal, which become even longer and even more frequent up to a fully irregular (or *chaotic*) condition. The investigation was carried out by considering a dynamical system subjected to one parameter variation (i.e., the Reynolds number) and it exploits some classical tools adopted in this field: phase maps, Poincaré sections and Lyapunov exponents. In particular, the Lyapunov exponents showed an oscillating trend in the range 3000–4000 and an asymptotic behavior for large Reynolds numbers. The same flow characteristics were also found on the Poincaré sections, obtained as planes in phase space for which the lift maxima are selected, where clustering and scattering of points correspond to periodic or irregular ranges, respectively.

ACKNOWLEDGMENTS

The research was developed within the Project Area Applied Mathematics of the Department of Engineering, ICT and Technology for Energy and Transport (DIITET) of the Italian National Research Council (CNR). The authors report no conflict of interest.

APPENDIX A: AUTOCORRELATION FUNCTIONS AND PSD FOR REYNOLDS RANGE 3200–10 000

In this Appendix the set of autocorrelation functions and PSD related to the Reynolds range 3200–10 000 is shown in Figs. 26 and 27.

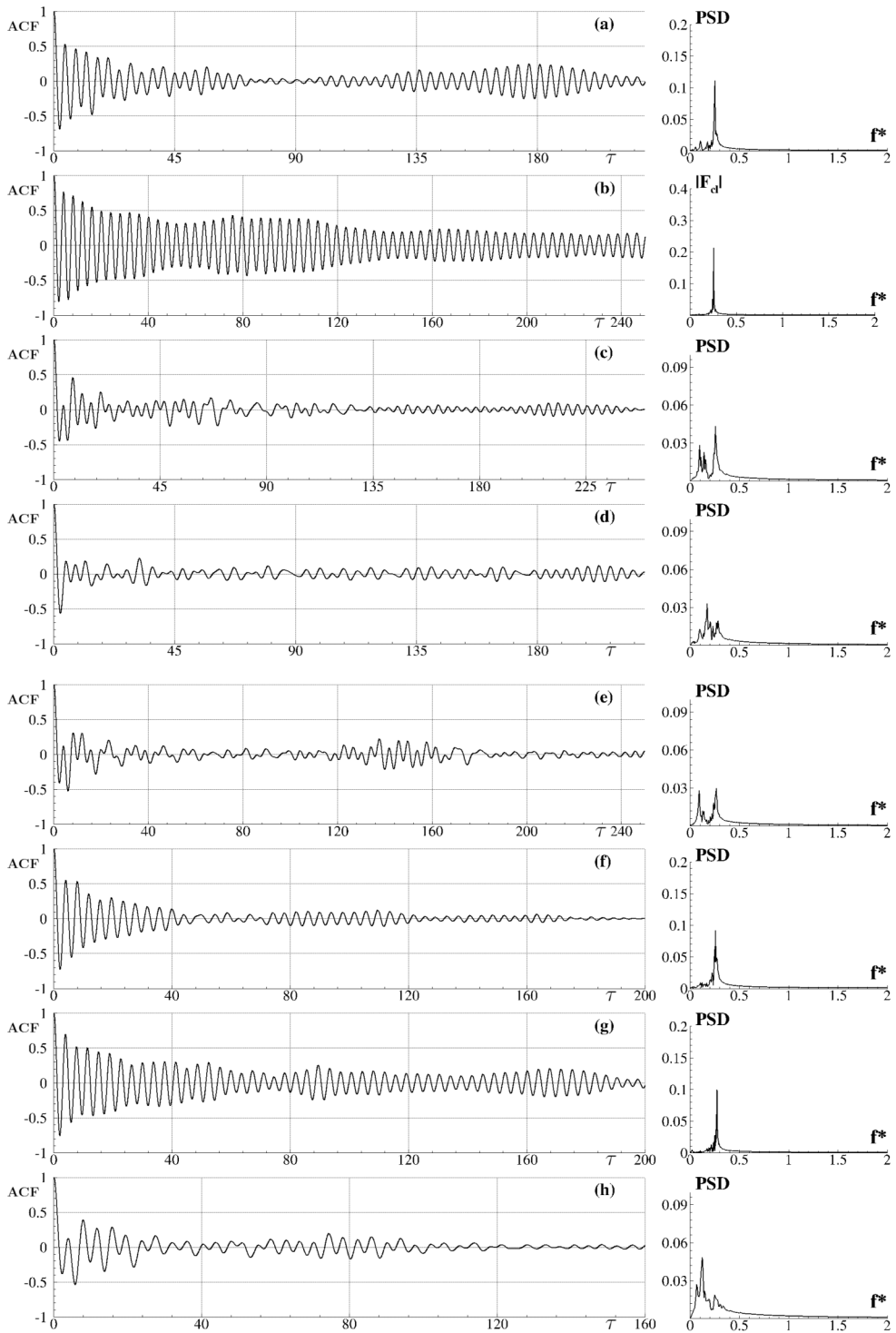


FIG. 26. Autocorrelation function (on the left frames) and power spectral density (on the right frames) for cases from $Re = 3200$ (top) to $Re = 3900$ (bottom). With τ the nondimensional time lag of the signal is indicated.

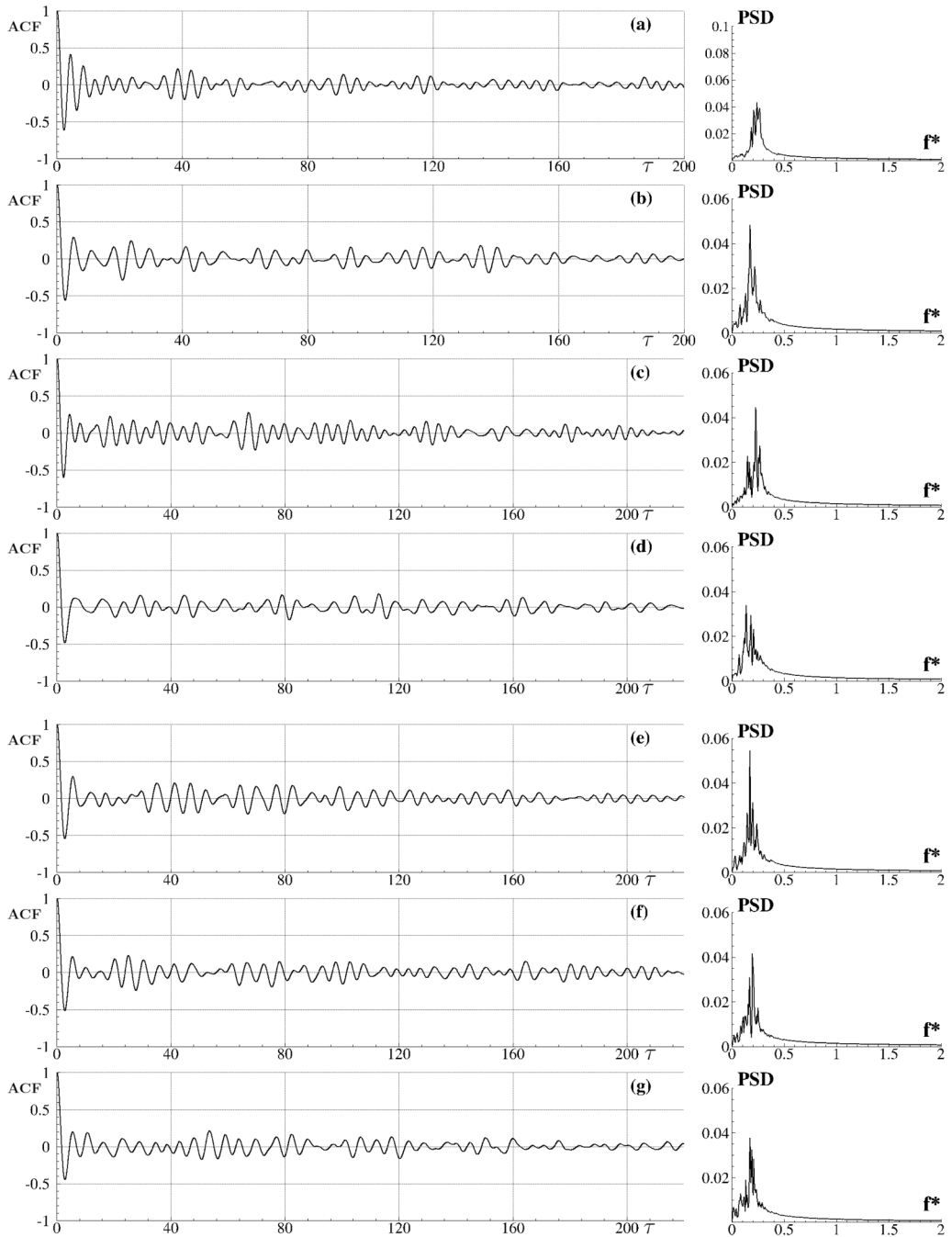


FIG. 27. Autocorrelation function (on the left frames) and power spectral density (on the right frames) for cases from $Re = 4000$ (top) to $Re = 10\,000$ (bottom). With τ the nondimensional time lag of the signal is indicated.

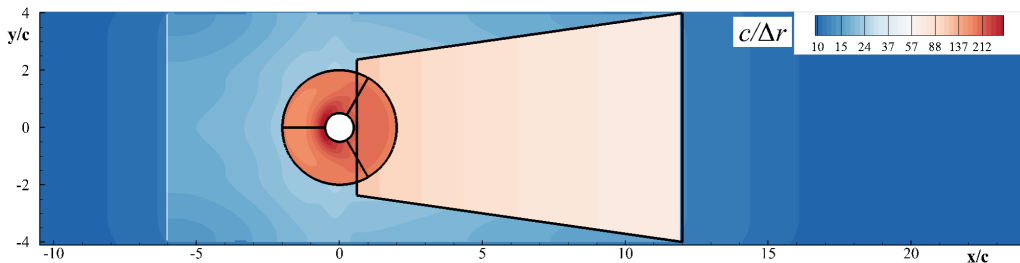


FIG. 28. Computational multiblock grid used for numerical simulations with FVM algorithm.

If f_i is the measurement of a random process at time t_i , and \bar{f} is the arithmetic average of the data between t_1 and t_N , then the autocorrelation function is defined as

$$ACF(\tau_k) = \frac{\sum_{i=1}^{N-k} (f_i - \bar{f})(f_{i+k} - \bar{f})}{\sum_{i=1}^N (f_i - \bar{f})^2}, \quad (\text{A1})$$

where τ_k is the data time lag [i.e., $k(t_i - t_{i-1})$], the denominator is the variance of the data multiplied by N and the data are assumed to be equally spaced.

As remarked in Secs. V and VII, the lift signal becomes less irregular for $Re = 3300$ and $Re = 3800$, so that a more regular and longer correlated function is expected. This is shown in the lines (b) and (g) of Fig. 26. The autocorrelation for $Re = 3300$ appears rather regular, with a PSD peak higher than all the others shown in this section, about half of the amplitude of the case $Re = 2000$ (comparing it with Fig. 9), thus indicating a general regularity of the shedding mechanism. Similarly, at $Re = 3700$ and 3800 , the signal appears more correlated. At $Re = 3700$ the correlation is observed for time lags up to 40, while the higher correlation of the 3800 case is related to the longer periodic ranges observed and discussed in Sec. VB, which are also responsible for one of the minima in the Lyapunov exponents trend, shown in Fig. 24.

When the Reynolds number increases, the autocorrelations become increasingly flat and also the small correlation range observed for short time lags (i.e., the signal is sufficiently regular to be self correlated for short time intervals) is almost absent. This means that the irregularity is so strong that any possible correlation of the signal, even for short times, is disrupted by the chaotic nature of the flow field.

APPENDIX B: COMPARISON WITH A FINITE VOLUME METHOD

In this Appendix, the cases $Re = 2000$ and $Re = 10\,000$ are simulated with a Finite Volume Method (FVM) and compared with the corresponding DVH ones. The comparison was carried out to assess whether the analyses of the lift time behavior, performed in the present paper, are independent of a specific numerical solver.

Unlike the DVH, the FVM works with a mesh-based approach and a multiblock decomposition of the numerical domain (more details can be found in Di Mascio [41], Di Mascio *et al.* [42]). The advective fluxes are discretized with an upwind third order scheme, while the time integration exploits a pseudocompressible approach.

Figure 28 sketches the multiblock grid used for the FVM simulations. The contour plot is representative of the spatial resolution $c/\Delta r$ characterizing the different zones of the domain, where Δr is the cubic root of the cell volume. The spatial resolution within the circular block around the cylinder is comparable with the DVH one, whereas a trapezoidal block is adopted for the wake region. The total number of cells is about 2 260 000.

At $Re = 2000$ a long period modulation on the time history of the forces was evidenced in Sec. IV. As shown in Fig. 29, the same time behavior is confirmed by the FVM simulations. Next

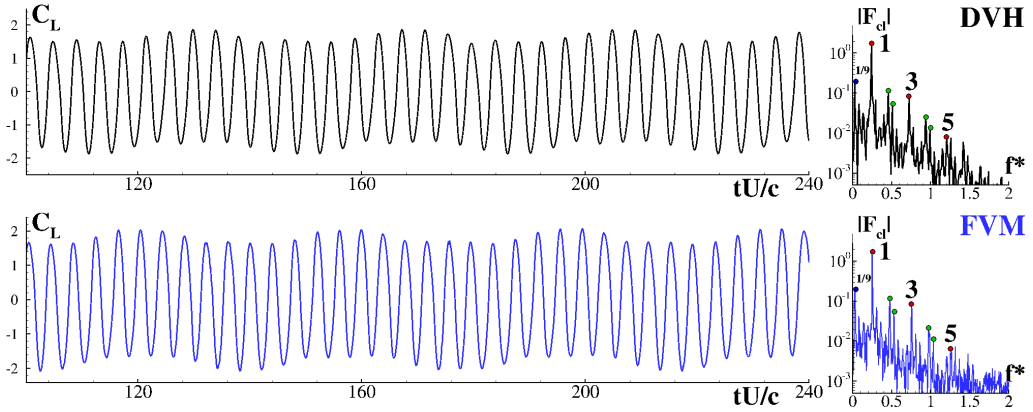


FIG. 29. Flow past a circular cylinder at $Re = 2000$: lift force comparison between DVH (top) and FVM (bottom) together with the corresponding Fourier transforms (right frames).

to the lift signals, the corresponding Fourier transforms are also depicted. As pointed out in Sec. IV, the spectrum peaks corresponding to integer multiples of the shedding frequency (indicated with the number 1) are highlighted with a red dot. The shorter peak at $1/9$ of the shedding frequency corresponds to the long period modulation and it is encountered in both simulations, as well as the irrational multiples of the main frequency (green circles).

In Fig. 30 the vorticity fields obtained by the FVM and DVH are compared at minimum lift conditions, showing a remarkable resemblance.

The chaotic behavior of the $Re = 10\,000$ case is also recovered in the FVM simulation, as can be seen in the time behavior of the lift signals, shown in Fig. 31. Figure 32 sketches a comparison between the vorticity fields. Considering the greater complexity of the solution to the highest Reynolds number studied, the solutions of the two solvers are still in satisfactory agreement.

APPENDIX C: A CRITERION FOR DEFINING REGULAR/IRREGULAR INTERVALS

In this Appendix a formal criterion for the definition of the regular/irregular time intervals based on the wavelet transform is given.

In the present work, a Morlet function is adopted with the symmetry parameter set to 3 and the time-bandwidth product equal to 60 (for more details see Ref. [43]). The modulus of the wavelet

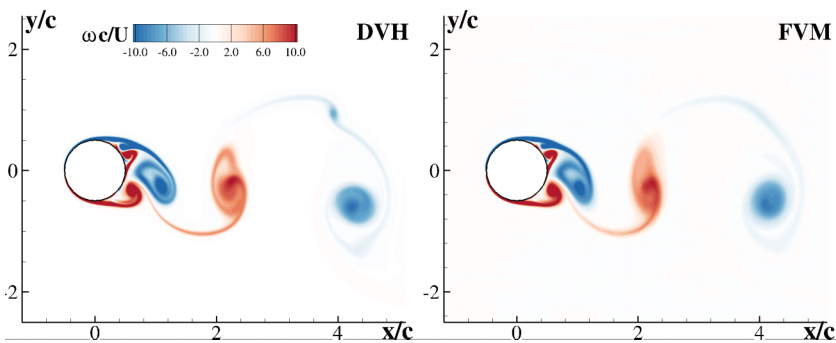


FIG. 30. Flow past a circular cylinder at $Re = 2000$: vorticity fields comparison between DVH (left) and FVM (right).

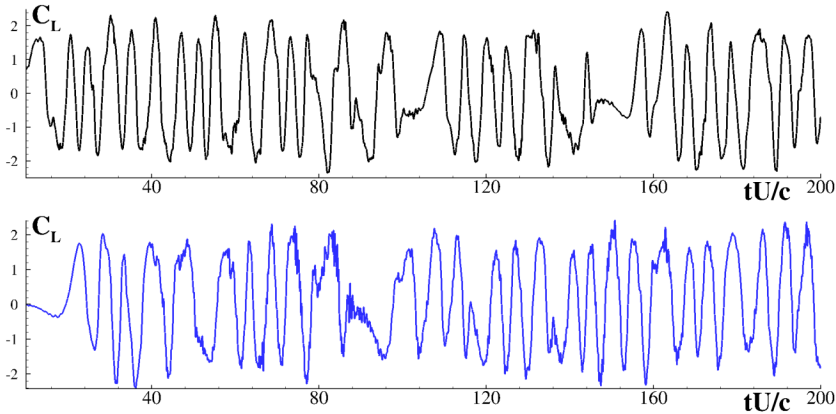


FIG. 31. Flow past a circular cylinder at $Re = 10\,000$: lift force comparison between DVH (top) and FVM (bottom).

coefficient is directly related to the amplitude of the time signal, in such a way that for a periodic signal the maximum is attained in correspondence of the carrier frequency.

In Fig. 33 the contour plots of wavelet coefficient amplitudes for $Re = 1000$, 3100 , and 3200 are sketched.

As discussed in Sec. III at $Re = 1000$ the lift signal is periodic and the wavelet transform returns a well defined banded contour (see top frame of Fig. 33). For $Re = 3100$ and $Re = 3200$, the time ranges where the maxima are attained are interspersed with other time ranges where the contour plot of the coefficient is irregular.

Different frequency intervals are identified through the contour lines corresponding to 95% of the maximum wavelet amplitude. Among those intervals the ones having a time range containing at least four lift oscillations are classified as *regular*. In the middle and bottom frames of Fig. 33 the different ranges are separated with vertical dash-dotted lines and numbered as the time signals shown in Sec. V.

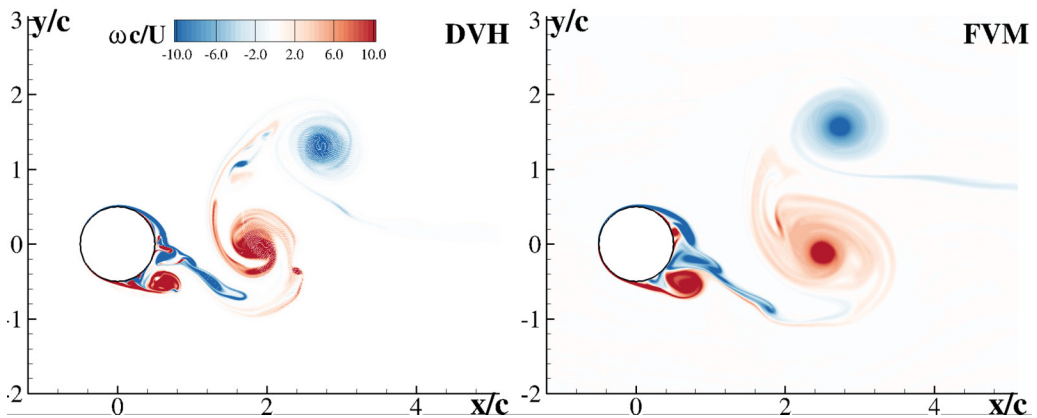


FIG. 32. Flow past a circular cylinder at $Re = 10\,000$: vorticity fields comparison between DVH (left) and FVM (right).

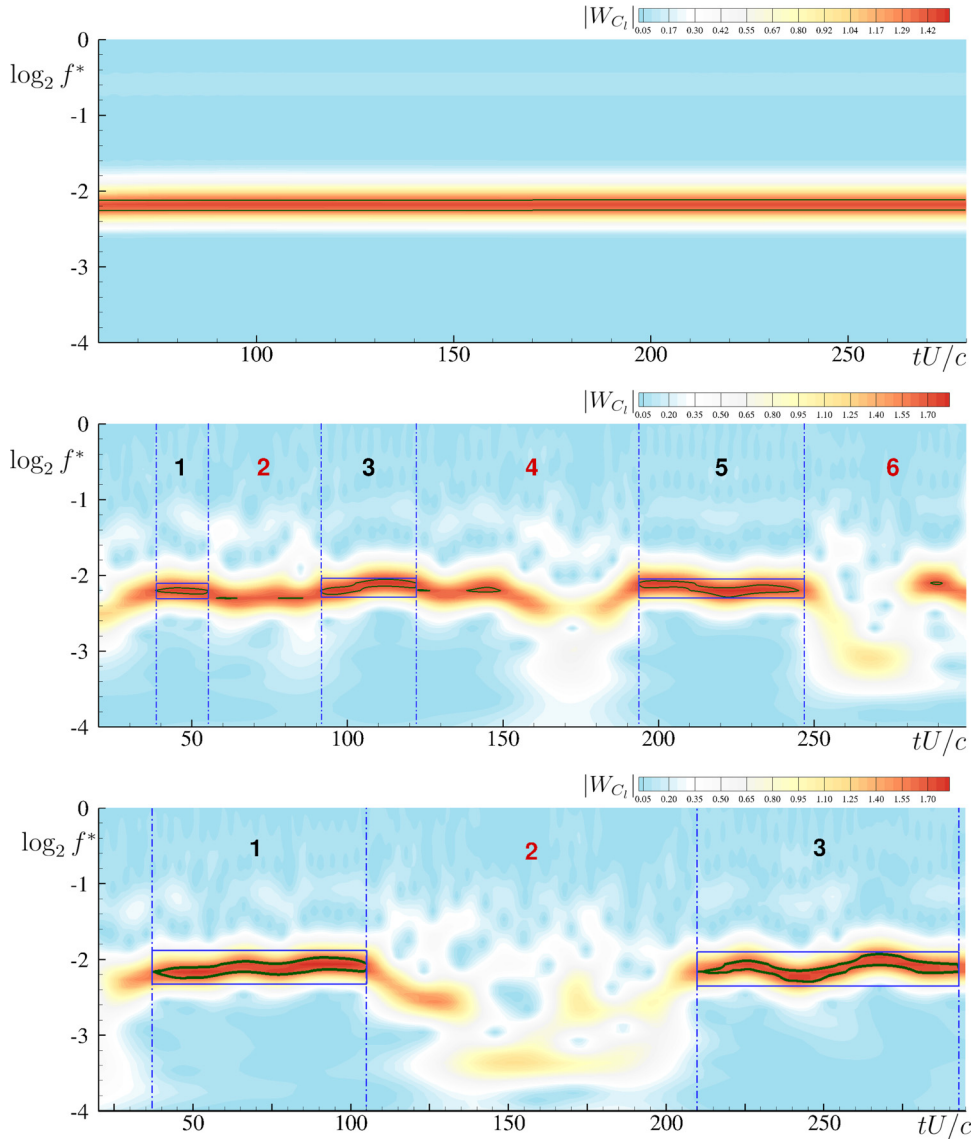


FIG. 33. Continuous wavelet transform with Morse wavelet for the lift signal at $Re = 1000$ (top), $Re = 3100$ (center), $Re = 3200$ (bottom). The contour lines correspond to 95% of the maximum wavelet amplitude.

- [1] M. Fayed, R. Portaro, A.-L. Gunter, H. A. Abderrahmane, and H. D. Ng, Visualization of flow patterns past various objects in two-dimensional flow using soap film, *Phys. Fluids* **23**, 091104 (2011).
- [2] T. Schnipper, A. Andersen, and T. Bohr, Vortex wakes of a flapping foil, *J. Fluid Mech.* **633**, 411 (2009).
- [3] L. Jia, Q. Xiao, H. Wu, Y. Wu, and X. Yin, Response of a flexible filament in a flowing soap film subject to a forced vibration, *Phys. Fluids* **27**, 017101 (2015).
- [4] S. Badrinath, C. Bose, and S. Sarkar, Identifying the route to chaos in the flow past a flapping airfoil, *Eur. J. Mech. B Fluids* **66**, 38 (2017).

- [5] C. Bose and S. Sarkar, Investigating chaotic wake dynamics past a flapping airfoil and the role of vortex interactions behind the chaotic transition, *Phys. Fluids* **30**, 047101 (2018).
- [6] A. Das, R. K. Shukla, and R. N. Govardhan, Existence of a sharp transition in the peak propulsive efficiency of a low-Re pitching foil, *J. Fluid Mech.* **800**, 307 (2016).
- [7] H. Krishnan, A. Agrawal, A. Sharma, and J. Sheridan, Near-body vorticity dynamics of a square cylinder subjected to an inline pulsatile free stream flow, *Phys. Fluids* **28**, 093605 (2016).
- [8] F. Mandujano and C. Málaga, On the forced flow around a rigid flapping foil, *Phys. Fluids* **30**, 061901 (2018).
- [9] P. Reichl, K. Hourigan, and M. C. Thompson, Flow past a cylinder close to a free surface, *J. Fluid Mech.* **533**, 269 (2005).
- [10] H. Ye, H. Wei, H. Huang, and X.-y. Lu, Two tandem flexible loops in a viscous flow, *Phys. Fluids* **29**, 021902 (2017).
- [11] M. Van Dyke and M. Van Dyke, *An Album of Fluid Motion* (Parabolic Press, Stanford, CA, 1982), Vol. 176.
- [12] M. M. Zdravkovich, *Flow Around Circular Cylinders: Fundamentals*, vol. 1 (Oxford University Press, Oxford, UK, 1997).
- [13] S. P. Singh and S. Mittal, Flow past a cylinder: Shear layer instability and drag crisis, *Int. J. Numer. Methods Fluids* **47**, 75 (2005).
- [14] D. Durante, E. Rossi, A. Colagrossi, and G. Graziani, Numerical simulations of the transition from laminar to chaotic behaviour of the planar vortex flow past a circular cylinder, *Commun. Nonlin. Sci. Numer. Simul.* **48**, 18 (2017).
- [15] D. Durante, O. Giannopoulou, and A. Colagrossi, Regimes identification of the viscous flow past an elliptic cylinder for Reynolds number up to 10000, *Commun. Nonlin. Sci. Numer. Simul.* **102**, 105902 (2021).
- [16] D. Durante, E. Rossi, and A. Colagrossi, Bifurcations and chaos transition of the flow over an airfoil at low Reynolds number varying the angle of attack, in *Communications in Nonlinear Science and Numerical Simulation* (Elsevier, Amsterdam, 2020), Vol. 89, p. 105285.
- [17] H. Jiang and L. Cheng, Transition to the secondary vortex street in the wake of a circular cylinder, *J. Fluid Mech.* **867**, 691 (2019).
- [18] G. Y. Dymnikova, Y. A. Dymnikov, and S. Guvernyuk, Mechanism underlying kármán vortex street breakdown preceding secondary vortex street formation, *Phys. Fluids* **28**, 054101 (2016).
- [19] T. H. Pulliam and J. A. Vastano, Transition to chaos in an open unforced 2D flow, *J. Comput. Phys.* **105**, 133 (1993).
- [20] A. K. Saha, K. Muralidhar, and G. Biswas, Transition and chaos in two-dimensional flow past a square cylinder, *J. Eng. Mech.* **126**, 523 (2000).
- [21] G. Graziani and P. Bassanini, Unsteady viscous flows about bodies: Vorticity release and forces, *Meccanica* **37**, 283 (2002).
- [22] E. Rossi, A. Colagrossi, B. Bouscasse, and G. Graziani, The diffused vortex hydrodynamics method, *Commun. Comput. Phys.* **18**, 351 (2015).
- [23] E. Rossi, A. Colagrossi, and G. Graziani, Numerical simulation of 2D-vorticity dynamics using particle methods, *Comput. Math. Appl.* **69**, 1484 (2015).
- [24] A. J. Chorin, Numerical study of slightly viscous flow, *J. Fluid Mech.* **57**, 785 (1973).
- [25] A. J. Chorin, Vortex sheet approximation of boundary layers, *J. Comput. Phys.* **27**, 428 (1978).
- [26] F. A. Cruz and L. Barba, Characterization of the accuracy of the fast multipole method in particle simulations, *Int. J. Numer. Meth. Engng.* **79**, 1577 (2009).
- [27] M. Benson, P. Bellamy-Knights, J. Gerrard, and I. Gladwell, A viscous splitting algorithm applied to low Reynolds number flows round a circular cylinder, *J. Fluids Struct.* **3**, 439 (1989).
- [28] L. Barba, A. Leonard, and C. Allen, Numerical investigations on the accuracy of vortex methods with and without remeshing, in *Proceedings of the 16th AIAA Computational Fluid Dynamics Conference* (AIAA, Reston, VA, 2003), p. 3426.
- [29] A. Colagrossi, B. Bouscasse, M. Antuono, and S. Marrone, Particle packing algorithm for SPH schemes, *Comput. Phys. Commun.* **183**, 1641 (2012).

- [30] A. Colagrossi, E. Rossi, S. Marrone, and D. Le Touzé, Particle methods for viscous flows: Analogies and differences between the SPH and DVH methods, *Commun. Comput. Phys.* **20**, 660 (2016).
- [31] O. Giannopoulou, A. Colagrossi, A. D. Mascio, and C. Mascia, Chorin approaches revisited: Vortex particle method vs finite volume method, *Eng. Anal. Bound. Elem.* **106**, 371 (2019).
- [32] E. Rossi, A. Colagrossi, D. Durante, and G. Graziani, Simulating 2D viscous flow around geometries with vertices through the diffused vortex hydrodynamics method, *Comput. Methods Appl. Mech. Eng.* **302**, 147 (2016).
- [33] E. Rossi, A. Colagrossi, G. Oger, and D. LeTouzé, Multiple bifurcations of the flow over stalled airfoils changing the Reynolds numbers, *J. Fluid Mech.* **846**, 356 (2018).
- [34] D. Sundararajan, *Fourier Analysis—A Signal Processing Approach* (Springer, Berlin, 2018).
- [35] N. Wiener, *Time Series* (MIT Press, Cambridge, MA, 1964).
- [36] D. F. Kurtulus, On the unsteady behavior of the flow around NACA0012 airfoil with steady external conditions at $Re = 1000$, *Int. J. Micro Air Vehicles* **7**, 301 (2015).
- [37] G. Birkhoff, Formation of vortex streets, *J. Appl. Phys.* **24**, 98 (1953).
- [38] Y. Tamura and G. Matsui, Wake-oscillator model of vortex-induced oscillation of circular cylinder, in *Wind Engineering* (Pergamon, Oxford, UK, 1980), pp. 1085–1094.
- [39] G. Riccardi and D. Durante, *Elementi di fluidodinamica: Un'introduzione per l'Ingegneria* (Springer Science & Business Media, Cham, 2007).
- [40] A. Wolf, J. B. Swift, H. L. Swinney, and J. A. Vastano, Determining Lyapunov exponents from a time series, *Physica D* **16**, 285 (1985).
- [41] R. Muscari, R. Broglia, and A. Di Mascio, An overlapping grids approach for moving bodies problems, in *Proceedings of the 16th International Offshore and Polar Engineering Conference (ISOPE'06)*, San Francisco, CA (International Society of Offshore and Polar Engineers, 2006).
- [42] A. Di Mascio, R. Broglia, and R. Muscari, On the application of the one-phase level set method for naval hydrodynamic flows, *Comput. Fluids* **36**, 868 (2007).
- [43] J. M. Lilly and S. C. Olhede, Generalized morse wavelets as a superfamily of analytic wavelets, *IEEE Trans. Signal Process.* **60**, 6036 (2012).
- [44] See Supplemental Material at <http://link.aps.org/supplemental/10.1103/PhysRevFluids.7.054701> for vorticity field evolution in the far and near fields at different Reynolds numbers.